PHYSICAL REVIEW FLUIDS **3**, 034601 (2018)

Contribution of large scale coherence to wind turbine power: A large eddy simulation study in periodic wind farms

Tanmoy Chatterjee[*] and Yulia T. Peet[†]
Integrative Simulations and Computational Fluids Lab, SEMTE, Arizona State University,
Tempe, Arizona 85287, USA

(Received 7 November 2016; published 5 March 2018)

Length scales of eddies involved in the power generation of infinite wind farms are studied by analyzing the spectra of the turbulent flux of mean kinetic energy (MKE) from large eddy simulations (LES). Large-scale structures with an order of magnitude bigger than the turbine rotor diameter (D) are shown to have substantial contribution to wind power. Varying dynamics in the intermediate scales (D–$10D$) are also observed from a parametric study involving interturbine distances and hub height of the turbines. Further insight about the eddies responsible for the power generation have been provided from the scaling analysis of two-dimensional premultiplied spectra of MKE flux. The LES code is developed in a high Reynolds number near-wall modeling framework, using an open-source spectral element code Nek5000, and the wind turbines have been modelled using a state-of-the-art actuator line model. The LES of infinite wind farms have been validated against the statistical results from the previous literature. The study is expected to improve our understanding of the complex multiscale dynamics in the domain of large wind farms and identify the length scales that contribute to the power. This information can be useful for design of wind farm layout and turbine placement that take advantage of the large-scale structures contributing to wind turbine power.

DOI: 10.1103/PhysRevFluids.3.034601

I. INTRODUCTION

Large organized arrays of wind turbines stretching over a span of tens of kilometers in the horizontal direction, commonly known as *wind farms* [1–3], have been conventionally used to extract wind energy from the atmospheric boundary layer (ABL) over the past two decades. Efficient design and operation of large wind farms not only requires the presence of high mean wind speed $\bar{U}$ (annual mean) at hub-height location, but also benefits from specific considerations regarding wind turbine position, e.g., the interturbine streamwise and spanwise distance, staggered versus aligned arrangements, etc. [4–8]. The dynamics of the power extraction by the wind turbines in a farm are very different and far more complicated than those of a stand-alone turbine [9–11]. As an example, our recent study [12] has revealed that large-scale structures with length scales of the order of ten turbine rotor diameters (D) made a significant contribution to the power generated by the wind turbines in a farm, which have not been observed so far in lone-standing turbines. While the presence of length scales $\sim D$ contributing to the turbine power in wind farms is intuitive and was reported recently [11,13], the current literature lacks an organized study on the contributions of still larger scales of motion ($\gg D$) in the wind farms.

---

[*] tchatte3@asu.edu
[†] ypeet@asu.edu

Large-scale structures near the wall are known to carry significant amounts of turbulent kinetic energy and Reynolds stresses in wall-bounded turbulence and were the subject of many recent studies in canonical and boundary layer flows [14–20], but not so much is known about the behavior of such structures in the region of wind turbine wakes. Understanding the physics of large-scale structures and their organization (coherence) influencing the wind turbines is important for characterization of wind turbine wake dynamics and power generation.

These structures can also potentially serve as an important metric apart from the hub-height mean wind speed in selecting land locations of wind farms.

Large wind farms are usually studied as *infinite wind farms* in the asymptotic limit [9,21,22], invoking streamwise-spanwise homogeneity through periodic boundary conditions. In this framework, the flow is "fully developed" and the wind turbine array imposes an additional *geometric roughness* $z_{0,\mathrm{hi}}$, and friction velocity $u_{*,\mathrm{hi}}$ (scales with streamwise–pressure gradient as $u_{*,\mathrm{hi}}^2/H = -\frac{1}{\rho}\partial p/\partial x$ [9]), which are higher than the bottom wall aerodynamic roughness $z_{0,\mathrm{lo}}$ and wall friction velocity $u_{*,\mathrm{lo}} = \sqrt{\tau_w/\rho}$ (τ_w is the wall-shear stress) imposed by the topography of the land [23–26]. The wind turbine array roughness $z_{0,\mathrm{hi}} \sim z_h/s_x s_y$ is influenced both by the turbine hub-height z_h, as well as nondimensional streamwise, spanwise turbine spacing parameters s_x, s_y ($s_x D, s_y D$ are the physical turbine spacings in multiples of the rotor diameter D). Analogous to the rough wall boundary layer flows, the concept of infinite wind farms provides a consistent way to study the influence of vertical physics in ABL turbulence due to the presence of wind turbines [9,12,27,28]. Previous literature have also illustrated the dominance of the vertical physics compared to the homogeneous horizontal counterpart in very large wind farms and have established that the vertical entrainment of mean kinetic energy (MKE) through turbulent shear stress flux, is responsible for the power generated by the turbines [9,21,22,28,29]. To the authors knowledge, there was only one recent study on large wind farms that commented on the presence of large-scale energetic counter-rotating roller modes in kinetic energy entrainment deduced by Proper Orthogonal Decomposition (POD) [30], despite the fact that large-scale organizations in MKE transport play a significant role in the power generated in large farms. In this work, we aim to analyze the physics of the large-scale structures in wind farms and investigate how they are influenced by the important farm design parameters, like wind turbine hub-height z_h, and the nondimensional streamwise, spanwise interturbine distances (s_x, s_y). It must be appreciated that the present work focuses on the global transport of the MKE flux in the computational domain, from the top wake region, $z_h + D/2$, to the bottom wake region, $z_h - D/2$, or vice-versa, and does not attempt to comment on how they correlate to the localized energy transfers in the wind turbine rotor region. This study is expected to improve the understanding of the MKE transport responsible for wind turbine power and the length scales involved, and also elucidate toward an efficient wind farm design that could position the wind turbines to systematically utilize the large-scale structures near and around them. The numerical studies in this work involving wind farms in ABL at $\mathrm{Re} \sim O(10^{10})$ are performed in a framework of large eddy simulations with near-wall modeling. The wind turbine forces are modeled using the state-of-the-art actuator line model [31], without resolving the turbine blades. Additionally, the use of periodic boundary conditions in our computations allows us to use Fourier transform in the horizontal directions and define the length scales (wavelengths) as the inverses of wave numbers k_x, k_y.

The rest of the paper is organized as follows. In Sec. II, we document the numerical methods, where we provide the details of the spectral element method and the large eddy simulation method with the near-wall modeling, followed by the description of the computational domain with the list of the LES simulations performed. In Sec. III, we present the results of the turbulent statistics in the periodic wind farms as well as the spectral analysis with the comments on the length scales involved in power generation. In Sec. IV, we discuss the conclusions from our key findings.

II. NUMERICAL METHODS

The numerical method implements a variational formulation of Navier-Stokes (NS) equations involving Galerkin projection using open-source spectral element solver Nek5000 [32] in $\mathbb{P}_N - \mathbb{P}_{N-2}$

formulation (see Ref. [33] for more details). The domain is partitioned into hexahedral elements in 3D, and within each element any variable can be expanded into a series of orthogonal basis functions (Lagrange-Legendre polynomials) with the grid points clustered toward the element boundaries known as Gauss-Lobato-Legendre (GLL) points, which are essentially the roots of the basis function polynomials. For smooth solutions, exponential convergence can be achieved with increasing order of the polynomials. The current algorithm was optimized to achieve perfect scalability in parallel implementation for up to 1 000 000 processors [32].

A. Subgrid-scale model for large eddy simulations

The spatially filtered 3D Navier-Stokes equations for LES of wind turbine arrays in neutrally stratified ABL flows can be obtained by incorporating a convolution integral filter on the original Navier-Stokes equations,

$$\frac{\partial \widetilde{\mathbf{u}}}{\partial t} + \widetilde{\mathbf{u}}\nabla\widetilde{\mathbf{u}} = -\frac{1}{\rho}\nabla \widetilde{p}^{*} + \widetilde{\mathbf{F}}_{x} + \widetilde{\mathbf{F}}_{\mathrm{AL}} + \nu\nabla^{2}\widetilde{\mathbf{u}} - \nabla \cdot \boldsymbol{\tau}. \tag{1}$$

Here, $\widetilde{\mathbf{u}}$ is the filtered velocity vector, $\widetilde{p}^{*}$ is the modified pressure [34], and $\widetilde{\mathbf{F}}_{x}$ is the streamwise driving pressure gradient, while $\widetilde{\mathbf{F}}_{\mathrm{AL}}$ represent the actuator line forces exerted by the rotating wind turbine blades. The subgrid stress (SGS) tensor in Eq. (1), $\boldsymbol{\tau} = \widetilde{\mathbf{u}\mathbf{u}^{T}} - \widetilde{\mathbf{u}}\widetilde{\mathbf{u}}^{T}$, arising from the noncommutativity of filtering with the nonlinear advection term, is modeled using an algebraic wall-damped Smagorinsky type eddy viscosity closure [35,36],

$$\boldsymbol{\tau}^{\mathrm{SGS}} - \tfrac{1}{3}\boldsymbol{\tau}^{\mathrm{SGS}}\delta_{kk} = -2(l_{f})^{2}|\nabla^{s}\widetilde{\mathbf{u}}|\nabla^{s}\widetilde{\mathbf{u}}, \quad \text{ł}_{f} = C_{s}\Delta, \tag{2}$$

where $\nabla^{s}\widetilde{\mathbf{u}} = 1/2(\nabla\widetilde{\mathbf{u}} + \nabla\widetilde{\mathbf{u}}^{T})$ and $|\nabla^{s}\widetilde{\mathbf{u}}| = (2\nabla^{s}\widetilde{\mathbf{u}} : \nabla^{s}\widetilde{\mathbf{u}})^{1/2}$. The grid size Δ in Eq. (2) is defined as $\Delta = (\Delta_{x}\Delta_{y}\Delta_{z})^{1/3}$ (Δ_{η} is the grid size in the η direction defined as the local average distance between the GLL nodes in this direction [36]), and the filter length scale is defined as $l_{f}^{-n} = (C_{s}\Delta)^{-n} = (C_{0}\Delta)^{-n} + [\kappa(z + z_{0})]^{-n}$ ($\kappa = 0.41$ is Von-Karman constant, $z_{0} = z_{0,lo}$), with $C_{0} = 0.19$, $n = 0.5$. The current model, through this specific choice of parameters $\{C_{0},n\}$, explores a new parametric function for the control of the filter length scales, that represents a slower growth with the distance from the wall than in classical models [23,24,35], which in fact exhibits a good fit with the growth of the filter length scales observed in dynamic models [23]. The proposed algebraic model can be viewed as a less expensive alternative to dynamic-based models that still provide reliable results in the calculations of the atmospheric flows, as is evident from the validation studies of the current model in the neutral atmospheric boundary layer simulations documented in Ref. [36].

B. Boundary conditions and near-wall model

We incorporate periodic boundary conditions in the streamwise and spanwise directions while the top boundary conditions are stress free. At the bottom surface, we use a wall stress boundary condition without having to resolve the rough wall, relating the wall stress vector $\boldsymbol{\tau}_{s}$ to the horizontal velocity vector $\widetilde{\boldsymbol{u}}_{h}$ at the first grid-point using the standard Monin-Obukhov similarity law [37] along with no-penetration conditions of large eddies, $\widetilde{w} = 0$,

$$\frac{1}{\rho}\boldsymbol{\tau}_{s} = -\kappa^{2}\frac{\widehat{\widetilde{\boldsymbol{u}}}_{h,\frac{\Delta z}{2}}(x,y,t)|\,\widehat{\widetilde{\boldsymbol{u}}}_{h,\frac{\Delta z}{2}}|(x,y,t)}{\log\left(\frac{z}{z_{0}}\right)\Big|^{2}_{\frac{\Delta z}{2}}}, \tag{3}$$

where $\widehat{\widetilde{\boldsymbol{u}}}_{h,\frac{\Delta z}{2}} = \widehat{\widetilde{u}}_{\frac{\Delta z}{2}}\vec{e}_{x} + \widehat{\widetilde{v}}_{\frac{\Delta z}{2}}\vec{e}_{y}$ ($\vec{e}_{x},\vec{e}_{y}$ are unit vectors in the x,y direction) and $|\widehat{\widetilde{\boldsymbol{u}}}_{h,\frac{\Delta z}{2}}| = \sqrt{\widehat{\widetilde{u}}^{2}_{\frac{\Delta z}{2}} + \widehat{\widetilde{v}}^{2}_{\frac{\Delta z}{2}}}$. The "hat" represents additional explicit filtering carried out in the modal space by attenuating $k_{c} = 4$ highest Legendre polynomial modes of the spectral element model [38], where k_{c} stands for the number of the highest modes being filtered. For collocated spectral element methods $\widehat{\widetilde{u}}_{\frac{\Delta z}{2}}$, $\widehat{\widetilde{v}}_{\frac{\Delta z}{2}}$ are calculated as an interpolation at half wall node $\Delta z/2$, i.e., between $\widehat{\widetilde{u}}(x,y,0,t)$ and $\widehat{\widetilde{u}}(x,y,z = \Delta z,t)$,

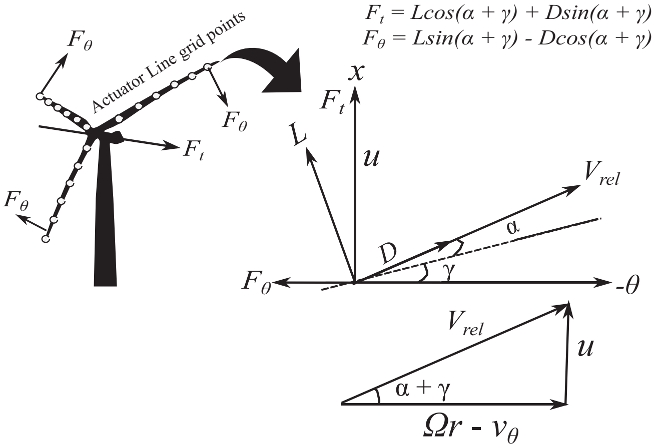

FIG. 1. Actuator line forces obtained at the nodal points of the turbine blades. $V_{\rm rel}$ is obtained from the velocity triangle. F_t and F_θ are the axial thrust and rotational forces on the turbine blades due to aerodynamic lift (L) and drag (D) forces.

where $\Delta\, z$ is the distance between the bottom boundary and the first GLL point from the boundary in the vertical direction. We ensure that $\Delta z/z_0 \gg 1$ to satisfy the assumptions and the similarity laws in the near-wall model [37,39–42].

To validate our spectral element near-wall LES model, the neutral ABL simulations have been conducted that have shown excellent logarithmic trends of the mean streamwise velocity in the inner layer ($z/H \leqslant 0.1$) when compared against the state-of-the-art scale dependent dynamic Smagorinsky model [23,24], and accurate $-1, -5/3$ scaling laws in the streamwise energy spectra. More technical details of the near-wall LES model and the specific choice of parameters can be found in Ref. [36]

C. Actuator line model

In an actuator line model [31], the blades with the aerofoil cross sections are divided into elements, similar to the blade element momentum theory (BEM), and the local lift (L) and drag (D) forces experienced by each element are calculated as $(L, D) = \frac{1}{2} C_{(l,d)}(\alpha)\, \rho\, V_{\rm rel}^2\, c\, w_d$, where c and w_d are the chord length and the blade width, respectively. The local angle of attack, α, is computed from the relative velocity, $V_{\rm rel}$, streamwise velocity, u ($\tilde{u}$ in LES) and the pitch angle, γ (Fig. 1). The lift and drag coefficients, $C_l(\alpha)$,$C_d(\alpha)$ of the aerofoil are tabulated beforehand from DNS or wind-tunnel experiments and are used in the computation of the local aerodynamic force $\vec{f} = L\vec{e_L} + D\vec{e_D}$ (here, $\vec{e_L}$ and $\vec{e_D}$ are the unit vectors in the direction of the local lift and drag, respectively). In the current paper, C_l,C_d were taken from the standard NACA aerofoil look-up tables [38]. The total reaction force from all the blade elements experienced by the fluid is distributed smoothly on several mesh points and is given as the actuator line force in the NS Eq. (1),

$$\widetilde{\mathbf{F}}_{\rm AL}(x, y, z, t) = -\sum_{i=1}^{N} \vec{f}(x_i, y_i, z_i, t)\, \eta_\epsilon(|\vec{r} - \vec{r}_i|), \tag{4}$$

$\vec{r} = (x,y,z)$, where $\eta_\epsilon(d)$ is a Gaussian function in the form of $\eta_\epsilon(d) = 1/\epsilon^3 \pi^{3/2} \exp\,[-(d/\epsilon)^2]$. The summation in the forces is over all N blade elements from the multiple wind turbine blades, and $\epsilon = 2\, w_d$ is used in the current study as suggested in Refs. [2,31] for optimum results. The AL model is more advanced than the actuator-disc model [9,22,30] commonly used in numerical computations of periodic wind farms, in its capability to capture the tip-vortices being shed in the near-wake quite accurately [31,38].

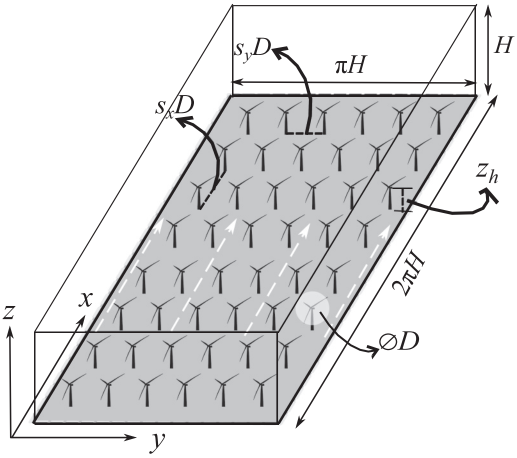

FIG. 2. Computational domain showing the 8 × 6 periodic arrangement of wind turbines for the baseline Case I. Hub height z_h, and rotor diameter D set to $0.1H$. The dashed white arrows indicate the direction of mean wind flow.

D. Computational setup

The computational domain utilized in this work to approximate the infinite wind farm setting is of rectangular geometry with dimensions $2\pi H \times \pi H \times H$ or $20\pi D \times 10\pi D \times 10D$ (H, D are the ABL thickness and the rotor diameter, respectively), as in Ref. [9] (see a schematic in Fig. 2 for details).

Wind turbines of fixed rotor diameter $D = 0.1H$ are placed in the computational domain as organized arrays. Table I documents the geometrical and computational parameters of the layout for the four cases simulated.

The Reynolds number $\mathrm{Re} = U_\infty H/\nu \sim 10^{10}$ has been set for all the cases, where U_∞ is the mean streamwise velocity at the top-edge of the boundary layer, which can be thought of as a representative of the geostrophic velocity in atmospheric flow driven by the pressure gradient and Coriolis forces [21,43]. Normalization with U_∞ was found to provide a meaningful comparison of variables between the different cases in the periodic wind farm setting.

Case I is considered as a baseline case with $s_x = 7.85, s_y = 5.23$, and a hub height $z_h = D = 0.1H$ located in the inner layer. Case I has been chosen as a standard test case considered in several other studies [8,9,30] and is consistent with the parameters of realistic wind farms in United States and Europe. Cases IIa and IIb (see Table I) will provide a way to study the influence of the streamwise and spanwise turbine distances on the large-scale structures in the MKE transport, while Case III

TABLE I. LES cases for the wind farm simulations. Domain size is $2\pi H \times \pi H \times H$ and $D = 0.1H$, fixed for all cases. N_{turb} is the number of turbines in streamwise-spanwise arrangement, N_i^e is the number of spectral element in the ith direction. N_{xyz} is the total number of grid points used in the computational domain. Grid of a neutral ABL simulation [36] is provided for comparison.

Case	N_{turb}	s_x	s_y	$s_x \times s_y$	s_x/s_y	$z_{0,\mathrm{Lett}}/z_0$	z_h	$N_x^e \times N_y^e \times N_z^e$	N_{xyz}
I	8 × 6	7.85	5.23	41.05	1.5	9.54	$0.1H$	54 × 56 × 24	2.52×10^7
IIa	4 × 6	15.7	5.23	82.11	3.0	4.77	$0.1H$	45 × 56 × 24	2.09×10^7
IIb	8 × 3	7.85	10.47	82.11	0.75	4.77	$0.1H$	54 × 44 × 24	1.98×10^7
III	8 × 6	7.85	5.23	41.05	1.5	31.5	$0.33H$	54 × 56 × 24	2.52×10^7
Neutral ABL	–	–	–	–	–	–	–	30 × 20 × 24	5.02×10^6

will contribute to our understanding of the MKE transport with a higher hub-height reaching into the outer layer ($z_h = 0.33H$), where the influence of the wall is diminished as compared to $z_h = 0.1H$. The bottom wall roughness $z_{0,lo} = z_0 = 10^{-4}H$ induced by topography is constant through all our simulation Cases I, IIa, IIb, and III. While the *geometric roughness* $z_{0,hi}$ as a function of (z_h, s_x, s_y) can be calculated from the LES simulation data, the geometric roughness by the wind turbines can also be *a priori* estimated from the roughness measure by Lettau [44], $z_{0,\text{Lett}} = z_h\pi/8s_xs_y$. A comparison of Lettau roughness normalized by the aerodynamic wall roughness, $z_{0,\text{Lett}}/z_0$ in Table I clearly indicates that the geometric roughness is an order of magnitude higher than its aerodynamic counterpart and is sensitive to the hub-height and turbine arrangements. Cartesian spectral element collocated grid has been used in the simulations, with the number of elements and the total grid count for each simulated case listed in Table I. All simulations were performed with seventh polynomial order of approximation, which required eight GLL collocation points per element per direction. The grids were constructed to satisfy some specific resolution requirements: (a) for the actuator line model, one requires on the order of four spectral elements along the actuator line in the yz rotor plane with the current GLL resolution; (b) one needs at least one spectral element to cover the distance of one rotor diameter downstream of each turbine in the x direction. These refinements are necessary in order to capture the helical vortices and the wakes shed by the rotating turbines downstream, and hence the number of turbines (see Table I) expectedly determines the grid requirements in the domain. Appendix A provides a more detailed documentation of the grid structure and grid resolution of the simulated cases.

The LES simulations as in Table I are computationally expensive requiring $\sim O(10^7)$ grid points and have been started with statistically stationary neutral ABL initial condition obtained from a separate precursor simulation. The wind turbine (WT) simulations have been run for long enough to allow the WT domain achieve temporal invariance in the statistical sense. After that, spatiotemporal snapshot data of velocities are collected for a span of $\sim 50T_e$ time ($T_e = 2\pi H/U_\infty$ is a flow-through time), which were used for spectral analysis involving Fourier transform.

III. RESULTS AND DISCUSSION

A. Statistics of infinite wind farms

The vertical variation of streamwise mean velocity profile for Cases I–III is shown in Fig. 3(a). The baseline Case I is validated against the actuator-disc LES simulations of Calaf *et al.* [9], illustrating the double log-layers as shown below:

$$\langle \overline{u}(z)\rangle = u_{*,lo}/\kappa \log(z/z_{0,lo}), \quad z < z_h - D/2, \tag{5}$$

$$\langle \overline{u}(z)\rangle = u_{*,hi}/\kappa \log(z/z_{0,hi}), \quad z > z_h + D/2. \tag{6}$$

Here, $u_{*,lo} = \sqrt{\tau_w/\rho}$ comes from the wall shear stress, while $u_{*,hi} = \sqrt{-\frac{H}{\rho}\partial p/\partial x}$ comes from the pressure gradient force. However, the friction scale velocities can also be approximated as $u_{*,lo} \approx \sqrt{-(\langle\overline{u'w'}\rangle + \langle\bar{u}''\bar{w}''\rangle)|_{z_h-D/2}}$ and $u_{*,hi} \approx \sqrt{-(\langle\overline{u'w'}\rangle + \langle\bar{u}''\bar{w}''\rangle)|_{z_h+D/2}}$. While the Reynolds stresses $\langle-\overline{u'w'}\rangle$ defined in the conventional way arise due to the correlation between u, w velocities, the dispersive stresses, $-\langle\bar{u}''\bar{w}''\rangle$, are a manifestation of the spatial heterogeneity of the u, w velocities, with $\langle\bar{u}''\rangle = \bar{u} - \langle\bar{u}\rangle$, $\langle\bar{w}''\rangle = \bar{w} - \langle\bar{w}\rangle$ ($^-$, temporal averaging; $\langle\rangle$, xy averaging). However, the dispersive stresses are usually much smaller than the Reynolds stresses in infinite wind farms. A comparison of the total stresses τ_{xz} (Reynolds + dispersive) for the different Cases I–III (Case I is also validated with Ref. [9]) is shown in Fig. 3(b). The comparison indicates that the differences in stresses in various wind turbine layouts for Cases I–III are more illustratively seen in the bottom wake region of the rotor manifesting the vertical energy entrainment. Since all the results involve the LES filtered variables, the tilde is dropped for brevity here and in subsequent plots and analysis.

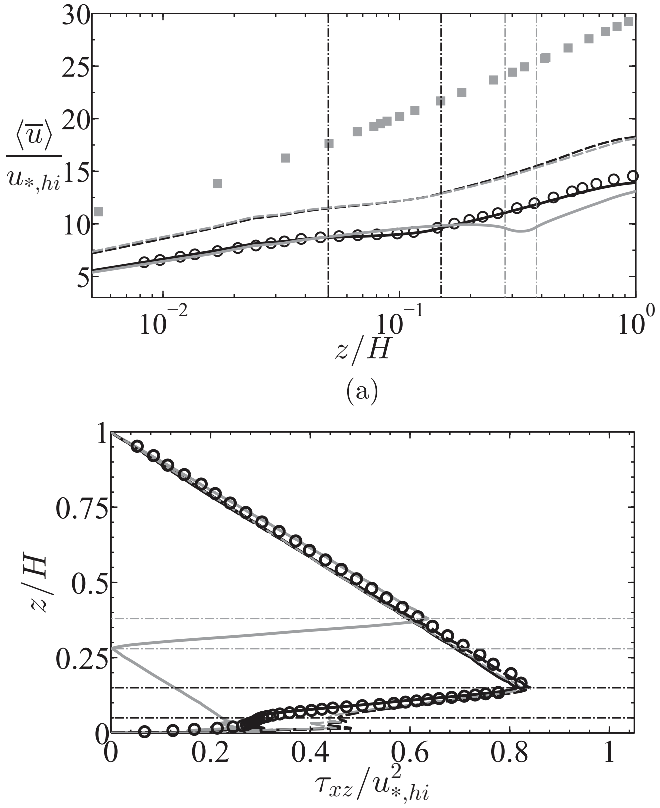

(a)

(b)

FIG. 3. (a) Mean streamwise velocity $\langle \overline{u} \rangle$ normalized by $u_{*,hi}$ vs. z/H. (b) Total (Reynolds + dispersive) stresses τ_{xz} normalized by $u_{*,hi}$ vs. z/H. Solid black—Case I, dashed black—Case IIa, dashed gray—Case IIb, solid gray—Case III. Solid gray □ in (a)—neutral ABL; open ○ in (a), (b)—Calaf *et al.* (2010) [9] (same wind farm setup parameters as in Case I). Black, gray dashed-dotted vertical (a) and horizontal (b) lines: rotor swept area of Cases I–III.

In infinite wind farms, the difference in turbulent shear stress (Reynolds + dispersive) flux component of the mean kinetic energy (MKE flux) at the top and bottom region of the rotor is responsible for the mean power per unit area generated by the wind turbines in the farm [6,9,21]. The MKE flux,

$$\Phi_p(z) = -(\langle \overline{u'w'} \rangle + \langle \bar{u}'' \bar{w}'' \rangle)\langle \overline{u} \rangle, \tag{7}$$

is plotted in Fig. 4(a) for all the Cases I–III. The MKE flux difference,

$$\Delta\Phi_p = \Phi_p(z_h + D/2) - \Phi_p(z_h - D/2), \tag{8}$$

was shown previously to correlate with the mean power density $\rho_{\text{mean}} \sim \Delta\Phi_p$ [9]. The mean power density, $\rho_{\text{mean}} = 1/(N_t s_x s_y D^2) \sum_{i=1}^{N_t} \bar{P}_i$, can be calculated by averaging the temporal mean power $\sum \bar{P}_i$ over all N_t turbines in the farm, and diving by the area $s_x D \times s_y D$. Fig. 4(b) manifests a strong correlation between $\Delta\Phi_p$ (MKE flux difference) and ρ_{mean} in the present data, confirming the findings in Ref. [9]. The present data also indicates that the mean power density roughly scales with the geometric turbine roughness in the regime of investigated s_x,s_y. It is understood however that such relationship is not supposed to hold once separation distances fall below a certain limit. As a

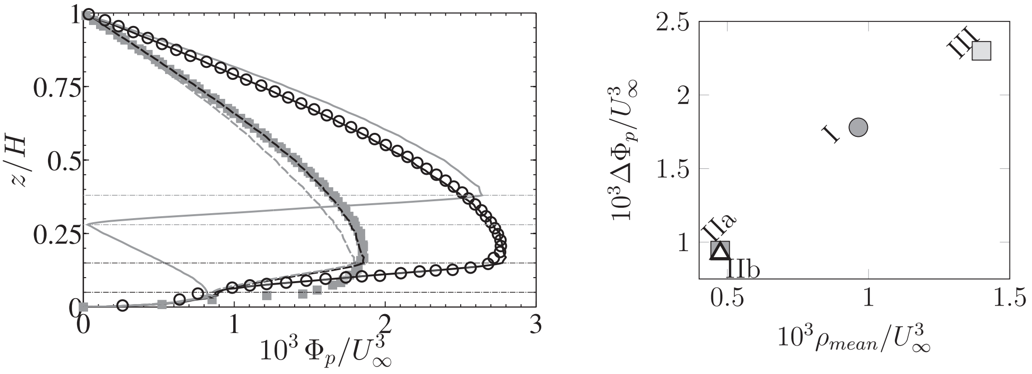

(a) (b)

FIG. 4. (a) Vertical variation of the MKE flux for different cases. Solid black—Case I, dashed black—Case IIa, dashed gray—Case IIb, solid gray—Case III. Gray square—neutral ABL. Open ○—Calaf *et al.* (2010) [9] (same wind farm setup parameters as in Case I). Dashed dotted lines: rotor swept area of Cases I–III. (b) Correlation between the difference in MKE flux $\Delta\Phi_p$ and mean power density ρ_{mean} for different cases.

reference, the temporal variation of the array-averaged power $P(t) = \frac{1}{N_t}\sum_{i=1}^{N_t}\bar{P}_i$ for different cases is plotted in Fig. 5.

B. Spectra of MKE flux

The spectra of the MKE flux $\Phi_p(z)$ and the MKE flux difference $\Delta\Phi_p$ defined in Eqs. (7) and (8) is of interest in this paper. The horizontal spectra of $\Phi_p(z)$ can be defined through the corresponding spectra of two-point correlations, see a more thorough discussion in Appendix B, as

$$\hat{\Phi}_p(k_x,k_y,z) = |\overline{\hat{u}(k_x,k_y,z)\hat{w}^*(k_x,k_y,z)}|\langle\overline{u}(z)\rangle, \tag{9}$$

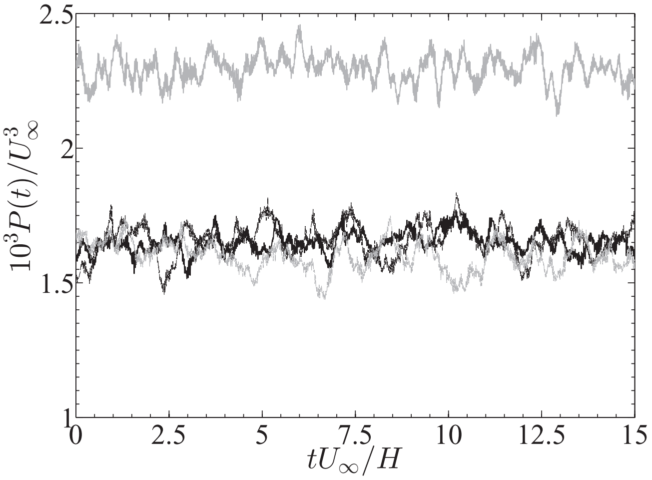

FIG. 5. Temporal variation of the array-averaged power $P(t) = \frac{1}{N_t}\sum_{i=1}^{N_t}\bar{P}_i$ of the turbines in different layouts. Solid black—Case I, dashed black—Case IIa, dashed gray—Case IIb and solid gray—Case III. Time scale is normalized with H/U_∞. Mean power gain: IIa/I—5%, IIb/I—2%, III/I—40%.

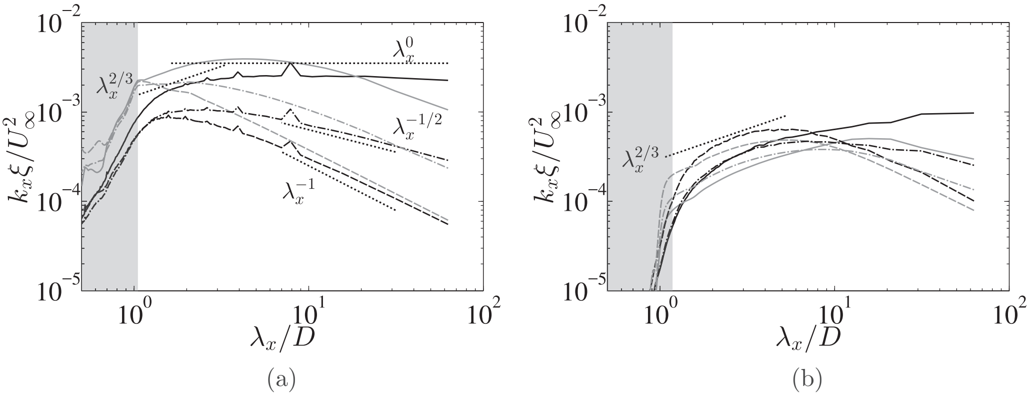

FIG. 6. Premultiplied 1D spectra $k_x\xi$ vs. normalized streamwise wavelengths λ_x/D for (a) $z = 0.25D$, (b) $z = 8.75D$. Black lines, Case I; gray lines, neutral ABL. k_xE_{uu} (–), k_xE_{ww} (−−), $k_x\phi_{uw}$ (−.−). All spectra normalized by U_∞^2. Gray patch corresponds to the resolved part of the spectra directly influenced by SGS viscosity.

where k_x, k_y are streamwise and spanwise wave numbers, $\widehat{}$ is the notation for the Fourier coefficients, and * refers to the complex conjugate. The horizontal spectra of the MKE flux difference can be defined accordingly,

$$\Delta\hat{\Phi}_p(k_x,k_y) = \hat{\Phi}_p(k_x,k_y,z_h + D/2) - \hat{\Phi}_p(k_x,k_y,z_h - D/2). \tag{10}$$

The Fourier coefficients can also be expressed as a function of streamwise, spanwise wavelengths, λ_x,λ_y ($\lambda_{x,y} = 2\pi/k_{x,y}$), and their integral in λ_x,λ_y space contributes to the full value,

$$\Delta\Phi_p = \int_0^\infty \int_0^\infty k_xk_y\Delta\widehat{\Phi}_p(\lambda_x,\lambda_y)d\log(\lambda_x)d\log(\lambda_y). \tag{11}$$

While Eq. (11) illustrates a cumulative effect of streamwise and spanwise length scales λ_x,λ_y on the MKE flux difference, we can still define its one-dimensional counterpart, using a 2D Fourier transform and integrating over one wavelength direction. Equation (12) shows the one-dimensional MKE flux difference spectra, $\Delta\widehat{\Phi}_p(\lambda_\eta)$, $\eta = x,y$, isolating the spectral content in the streamwise and spanwise length scales, respectively,

$$\Delta\widehat{\Phi}_p(\lambda_\eta) = \int_0^{\lambda_{\zeta,\max}} \Delta\widehat{\Phi}_p(\lambda_\eta,\lambda_\zeta)d\lambda_\zeta, \tag{12}$$

where $\eta = x$, $\zeta = y$, and vice-versa. Equation (13) below defines the cumulative spectral content of the 1D MKE flux difference in streamwise and spanwise length scales. For example, $\gamma_x(\lambda_0)$ shows the fraction of MKE flux difference, contained at length scales $\lambda_x \geqslant \lambda_0$ and $\gamma_\eta(0) = 1$,

$$\gamma_\eta(\lambda_\eta) = \frac{\int_{\lambda_\eta}^\infty \Delta\widehat{\Phi}_p(\lambda'_\eta)d\lambda'_\eta}{\int_0^\infty \Delta\widehat{\Phi}_p(\lambda'_\eta)d\lambda'_\eta}, \quad \forall\eta = x,y. \tag{13}$$

In the near-wall regime, robust scaling laws of the *attached eddies* [45,46] can be observed in wind farms. For example, Case I in Fig. 6(a) shows the existence of the k_x^{-1} scaling (λ_x^0 scaling in premultiplied spectra) in the u energy spectra, which are manifestations of the overlap region of the scales of attached eddies with the integral length scales [36,47,48]. The $k_x^{-1/2}$ scaling law ($\lambda_x^{-1/2}$ in premultiplied spectra) of ϕ_{uw} (cospectra) is an illustration of the near-wall organizations of Reynolds-stress carrying structures, as demonstrated in the correlation scaling of 1D spectra [36,49],

$$\phi_{uw} \approx E_{uu}^{1/2}E_{ww}^{1/2}, \tag{14}$$

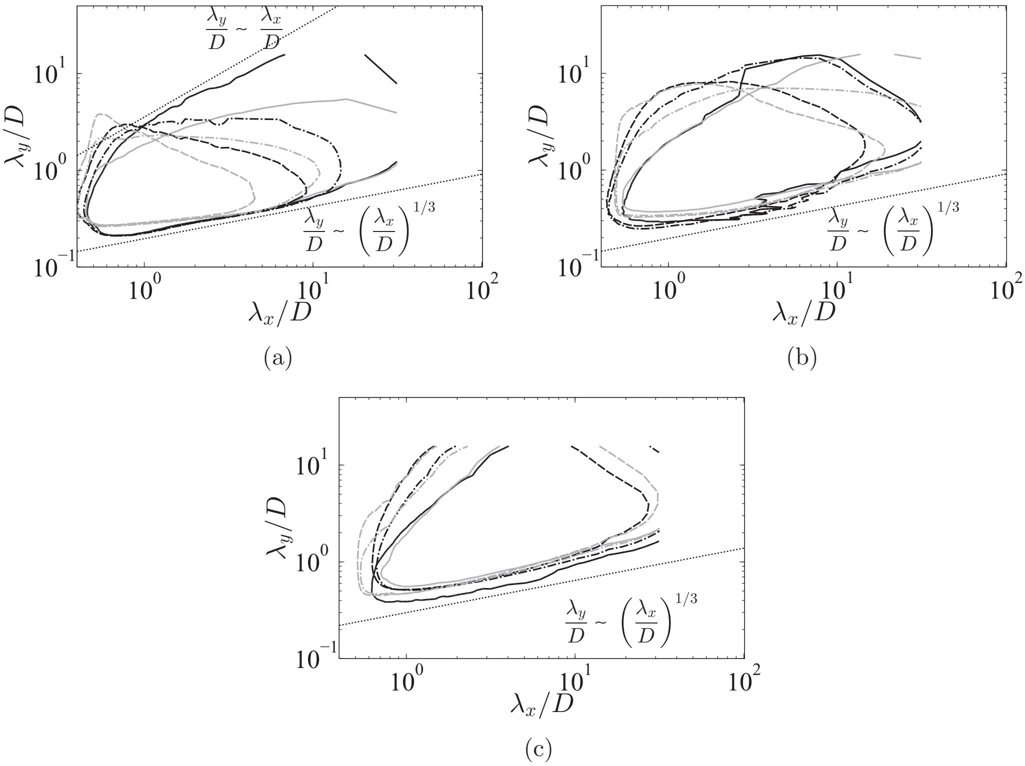

(a)

(b)

(c)

FIG. 7. 2D premultiplied energy spectra vs. normalized streamwise and spanwise wavelengths, λ_x/D, λ_y/D. Black lines, Case I; gray lines, neutral ABL. $k_x k_y E_{uu}$ (–), $k_x k_y E_{ww}$ (– –), $k_x k_y \phi_{uw}$ (–.–). (a) $z = 0.25D$ (b) $z = D$ (c) $z = 8.75D$. Contours are 0.25 of maximum at that level. All spectra normalized by U_∞^2.

with $E_{uu} \sim k_x^{-1}$ and $E_{ww} \sim k_x^0$ [see Fig. 6(a)]. Here $\phi_{uw} = \overline{|\hat{u}\hat{w}^*|}$, $E_{uu} = \overline{\hat{u}\hat{u}^*}$, and $E_{ww} = \overline{\hat{w}\hat{w}^*}$, where hat represents the Fourier transform and $*$ represents the conjugate transpose. These correlated scaling regions were observed throughout the inner layer $z < D$. In 1D scenario, e.g., for variation only in λ_x, integration of the spectral variables $E_{uu}, E_{ww}, \phi_{uw}$ has been performed in the λ_y direction. When compared to neutral ABL simulations (without wind turbines), we observe similar scaling laws, but for the wind turbine domain, the attached eddy scaling laws extend to larger length scales $\lambda_x > 10D$. This observation is further corroborated in the 2D premultiplied spectra shown in Fig. 7. The figure also illustrates that the vertical w spectra of wind farms at close to the wall locations, $z < D$, as well as u spectra and a cospectra at the same contour level, extend to much larger streamwise and spanwise length scales compared to the neutral ABL. This indicates that the 3D turbulent motions also increase in size near the wall, possibly due to the vertical entrainment of the *mean kinetic energy flux* in wind farms, which requires *downdrafts* or vertical motions from the high-speed regions above the turbine rotor toward the wall [12,50]. Note that the higher locations in the boundary layer, e.g., at $z = D$ and $z = 8.75D$, do not show this feature, as can be seen from the corresponding premultiplied spectra plots.

In general, Fig. 7 shows good trends of the linear dispersion, $\lambda_y \sim \lambda_x$ in the u spectra, corresponding to the *active wall-normal motions* as well as the power law scaling, $\lambda_y \sim \lambda_x^{1/3}$ in both u, w energy spectra and the $\overline{u'w'}$ cospectra corresponding to the *attached inactive motions* [51,52]. However, it must be appreciated that the $1/3$ law scaling, unlike the wall-bounded turbulence [36,49], has its contribution both from the low-speed streaks near the wall, as well as from the spanwise

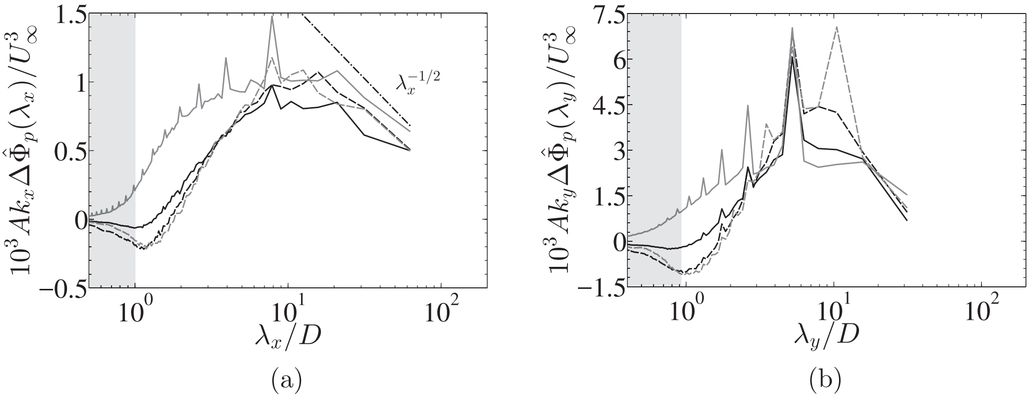

(a)

(b)

FIG. 8. One-dimensional normalized premultiplied difference in the MKE flux spectra $k_\eta \Delta\hat{\Phi}_p(\lambda_\eta)$ [Eq. (12)]between the top and bottom wake region, $z = z_h \pm D/2$: (a) versus streamwise wavelength, $\eta = x$; (b) versus spanwise wavelength, $\eta = y$. Solid black—Case I; dashed black—Case IIa, dashed gray—Case IIb; solid gray—Case III. $A = s_x s_y D^2$. Gray patch—resolved part of the spectra directly influenced by SGS viscosity.

modulation of the velocities due to the wind turbine wakes as shown later in Eq. (16). Similar near-wall scalings are observed in other cases (not shown here).

Figures 6(a) and 6(b) show that a considerably long region of the $-5/3$ law ($\lambda_x^{2/3}$) is present in the 1D spectra in the neutral ABL case at scales $\lambda_x > D$. These scales are adequately resolved by the grid as evident from the details of the grid resolution presented in Appendix A. At scales lower than D, $\lambda_x < D$, the drop in spectra is noticeable, which is explained by the fact that, although the scales down to $\sim 0.6D$ are still resolved by the grid (see Appendix A 2), they are also effected by the subgrid scale viscosity, since they correspond to the highest resolved wave numbers targeted by the subgrid scale dissipation. These scales are identified by gray patches in Figs. 6(a) and 6(b), following Ref. [53]. It can also be observed, that in neutral ABL, the decay rate of the spectrum at $\lambda_x < D$ is different in the inner and outer layer owing to decreasing eddy viscosity effects near the wall. The extent of the $-5/3$ law is smaller in wind turbine simulations that in the neutral ABL. Since these deviations are observed in the region of scales that are well resolved in both cases with and without wind turbines, this fact provides a room for hypothesis that the observed effect might be caused by the modulation of turbulence by wind turbines.

Figure 8 shows the spectral content of $k_x \Delta\widehat{\Phi}_p(\lambda_x)$, $k_y \Delta\widehat{\Phi}_p(\lambda_y)$, the one-dimensional premultiplied spectral surrogates to the difference in MKE flux ($\Delta\Phi_p$), which illustrates the contribution of streamwise and spanwise length scales in the mean power generated by the wind turbines. It must be noted that the spectra $k_\eta \Delta\widehat{\Phi}_p(\lambda_\eta)$ have been further multiplied by $A = s_x s_y D^2$, which enables us to compare the mean power $P_{\text{mean}} = \rho_{\text{mean}} A$ of the turbines in the wind farm, instead of the mean power density. Although it might be slightly obscured in the premultiplied spectra plot of the Fig. 8, where differences in smaller length scales are artificially exaggerated by multiplying by higher values of k_x, k_y, the largest discrepancies in the spectra and hence wind turbine power among different Cases I–III come from the larger length scales $\lambda_x, \lambda_y > 10D$. It is clearly seen from the corresponding spectra plots that are not premultiplied by wave numbers (not included here). We do admit that larger length scales might also suffer from large uncertainties when it comes to their spectral characteristics due to their larger coherence times and a potential lack of a sufficient number of uncorrelated samples. In a separate uncertainty analysis of the MKE flux difference spectra at large length scales to the duration of the averaging time, it was concluded that the statistical uncertainty is less than 0.01% with the current averaging of 50 flow through times, both for the streamwise and the spanwise spectra. Additionally, we also observe the presence of *negative contribution* of $k_x \Delta\widehat{\Phi}_p(\lambda_x)$, $k_y \Delta\widehat{\Phi}_p(\lambda_y)$ in Cases I, IIa, and IIb (corresponding to the lower hub-height of $z_h = 0.1H$, which is also equal to D)

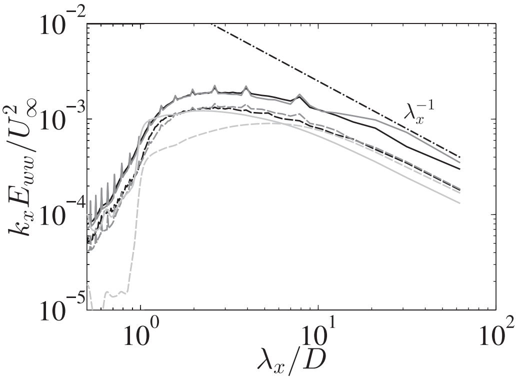

FIG. 9. One-dimensional premultiplied vertical velocity spectra $k_x E_{ww}$ at $z = z_h + D/2$ vs. normalized streamwise wavelength λ_x/D with and without wind turbines. Solid black—Case I; dashed black—Case IIa, dashed gray—Case IIb; solid gray—Case III. Solid light gray—neutral ABL, rotor region of I. Dashed light gray—neutral ABL, rotor region of III. Gray patch—resolved part of the spectra directly influenced by SGS viscosity.

for streamwise and spanwise length scales in the order of turbine rotor diameter D. This negative contribution corresponds to the upward transfer of the MKE flux from the bottom to the top wake region, that does not contribute to the turbine power. It might be hypothesized that the updrafts in the small scales of motion are associated with the near-wall turbulence bursts that reach wind turbines with relatively low hub-heights of $z_h = D$. While the contribution to the flux difference at smaller length scales $\lambda_x,\lambda_y \sim O(D)$, is negative for Cases I, IIa, and IIb, it is observed that Case III corresponding to the higher hub-height of $z_h = 0.33H$ still contributes to 15% of $\Delta\widehat{\Phi}_p(\lambda_x)$ and 20% of $\Delta\widehat{\Phi}_p(\lambda_y)$, in those scale ranges. Since wind turbines now are three times higher ($z_h = 3D$), the near-wall energetic motions do not reach the turbine rotor region any longer. It is suspected that the contribution to the power by the intermediate length scales $\sim D$ in Case III mainly comes from the incoherent yet energetic outer scales of motion [52]. This can also be seen in the vertical spectra at $z = z_h + D/2$ in Fig. 9. The vertical spectra manifests the potential turbulent vertical motions ("downdrafts") due to the entrainment of mean kinetic energy, and when compared to neutral ABL data provides interesting revelations. At $z = z_h + D/2$, the differences in the neutral ABL and WT spectra (Cases I, IIa, and IIb) occurs at $\lambda_x > 10D$, while for Case III, the discrepancies can be seen at scales $\lambda_x > D$ in the outer layer, all of which contribute to the turbine power.

Peaks in the spectral flux difference $k_\eta \Delta\widehat{\Phi}_p(\lambda_\eta)$, $\eta = x,y$ (Fig. 8), are observed, corresponding to $\lambda_x = m s_x D$, $m = 1,2,\ldots$ in the streamwise scaling and $\lambda_y = n s_y D$, $n = 1,2,\ldots$ in the spanwise scaling, which are illustrative of the periodicity imposed by the repeated turbine arrangements in the farm.

At length scales $\lambda_x \sim O(10^2 D)$, the $k_x^{-1/2}$ law of *attached eddies* ($\lambda_x^{-1/2}$ in the premultiplied spectra) can still be observed in all the cases. This is primarily because of the fact that the $-1/2$ scaling law is also observed at similar λ_x locations in both the top and bottom MKE flux; see Fig. 10. Peaks corresponding to wind turbine placement are also observed in both the top and bottom MKE flux.

Another interesting phenomenon observed is the difference in the spectra in the Cases I, IIa, and IIb (different interturbine distances s_x,s_y), where the wind turbines have the same hub-height z_h, and hence potentially would have the access to similar large-scale structures in the logarithmic layer [18,19,54]. The array-averaged turbine power ($\rho_{\text{mean}} s_x s_y D^2$) in Cases IIa and IIb is slightly higher than in Case I (see Fig. 5), due to a better wake recovery owing to less number of turbines per unit area [6,10]. Cases I, IIa, and IIb demonstrate a completely different dynamics at streamwise and spanwise length scales larger than D, below which the SGS dissipation is dominant. For example, at

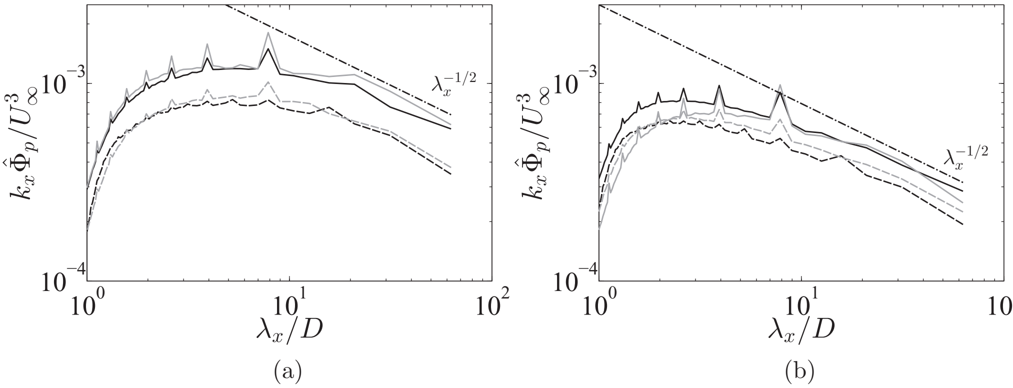

FIG. 10. One-dimensional premultiplied MKE flux spectra $k_x\hat{\Phi}_p$ versus normalized streamwise wavelength: (a) at the top wake region $z = z_h + D/2$; (b) at the bottom wake region $z = z_h - D/2$. Solid black—Case I; dashed black—Case IIa, dashed gray—Case IIb; solid gray—Case III.

higher $s_x \times s_y$, Cases IIa and IIb compared to Case I manifest higher magnitudes of updrafts at scales $\sim D$ and subsequently larger magnitudes of MKE flux downdrafts at scales $>10D$ as well, which might be related to a diminished effect of wake interference, otherwise inhibiting energetic near-wall updrafts and outer layer downdrafts. It must be noted that, when integrated over all length scales, a relative surplus in positive and negative contributions in Cases IIa and IIb partially cancels out, subsequently providing comparable values of power in Cases I, IIa, and IIb. The fact that the spectral content of the MKE flux difference (Fig. 8) is quite different at different length scales provides a room for a hypothesis that the arrangements of wind turbines (s_x, s_y) actually modulate the large-scale organizations in the log layer. From the spectra of Cases I, IIa, and IIb [Figs. 8(a) and 8(b)], it is thus clear that increasing s_x allows the wind farm to take advantage of much larger streamwise structures, since in Case IIa, contribution to mean power is the highest for length scales $>10D$. Increasing s_y allows for wider structures $(\lambda_y > \lambda_x)$ to contribute to the farm power [Fig. 8(b)], but streamwise horizontally anisotropic motions are more energetic than their spanwise counterparts [19], thus the spectral power contribution (MKE flux difference) in Case IIb at length scales $\lambda_x < 10D$ [Fig. 8(a)] is larger than in Case IIa.

The modulation of large-scale structures can be further understood from the visualization of the isosurfaces (Case I) of streamwise velocity at 65% and 95% of U_∞ in Fig. 11, depicting the region $z < z_h + 0.75D$. The isosurface plot shows that the presence of wind turbines generate the more energetic patches, $u = 0.95U_\infty$, propagating downstream, in between the surfaces of $u = 0.65U_\infty$, which are not prominently seen in the neutral ABL flow, without the turbines.

While the above discussion provides a qualitative visualization, a quantitative aspect of the modulation of large-scales structures can be observed from the plots of integral length scales, which demonstrate a measure of *correlated large scales* of motion. Figure 12(a) shows the variation of integral length scales $\mathfrak{L}_{uu}$ with wall-normal distance, the definition of the integral length scale used in the current study being given in Appendix C. Since the integral length scales are bounded by $30D$ in all cases, which is less than half of the largest resolved streamwise wavelength $L_x = 20\pi D$ imposed by the domain length, one can conclude that the computed integral length scales are not numerically influenced by the imposed periodicity of the domain. It is interesting to observe that the integral scales in Cases I, IIa, IIb, III and the neutral ABL without turbines are more or less similar in the outer layer but manifest a marked difference in the inner layer and at hub-height. This also corroborates that the modulation of the structures in wind farms are not only caused by the direct turbulence-turbine interaction at hub-heights but also due to the “downdrafts” of the MKE flux as also analyzed in Fig. 8. The integral length scales in Fig. 12(a) and the mean-squared streamwise velocity fluctuations $\overline{u'^2}/U_\infty^2$ both indicate that peaks occur at the hub-height of the turbines in the

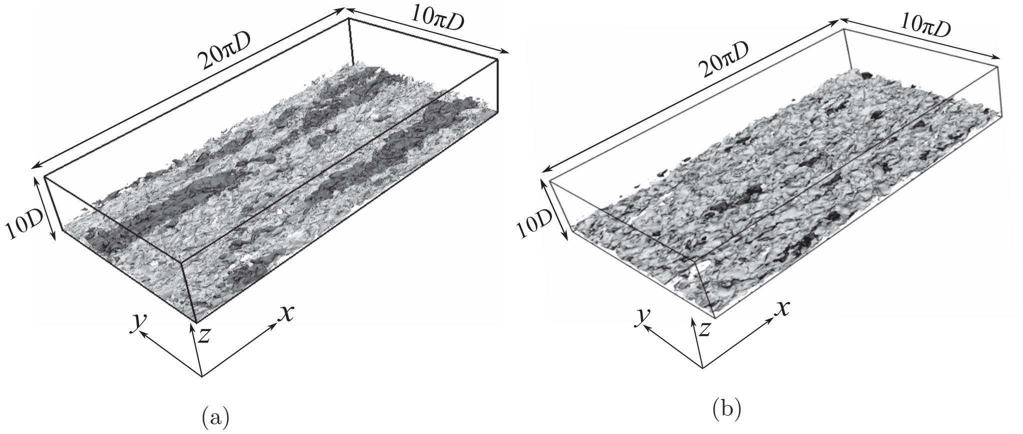

FIG. 11. Modulation of large-scale structures. Isosurface of normalized velocity magnitude $\sqrt{u^2+v^2+w^2}/U_\infty$ for $z \leqslant z_h + 0.75D$. (a) Wind turbine array, Case I. (b) neutral ABL, without wind turbines. Light gray patch—$0.65U_\infty$, dark gray patch—$0.95U_\infty$.

wind farm. Between Cases I, IIa, and IIb, which are at the same hub-height, the integral length scales in the bulk of the boundary layer grow in magnitude as s_x/s_y is decreased. When Cases I and IIa are compared, which have the same s_y but different s_x, Case IIa with the smaller streamwise turbine separation manifests larger length scales, since the streamwise wakes of the concurrent turbines effectively merge producing longer structures, while they have more time to recover and mix before hitting the downstream turbines in Case I. Similarly for a fixed s_x, increasing s_y from Case I to IIb allows the correlated structures in the wakes to grow more with smaller spanwise interference. Case III at a higher hub-height $z_h = 0.33H$ (outer layer) manifests a peak of a similar magnitude at hub-height as Case I with the same s_x, s_y, showing a consistent trend in the influence of the turbine separation distances on the peak integral length scales, irrespective of the hub-height. While the vertical diffusion of length scales from the hub-height location might seem smaller in Case III in Fig. 12(a), this is due to the logarithmic scaling of z axis and is, in effect, similar between all the

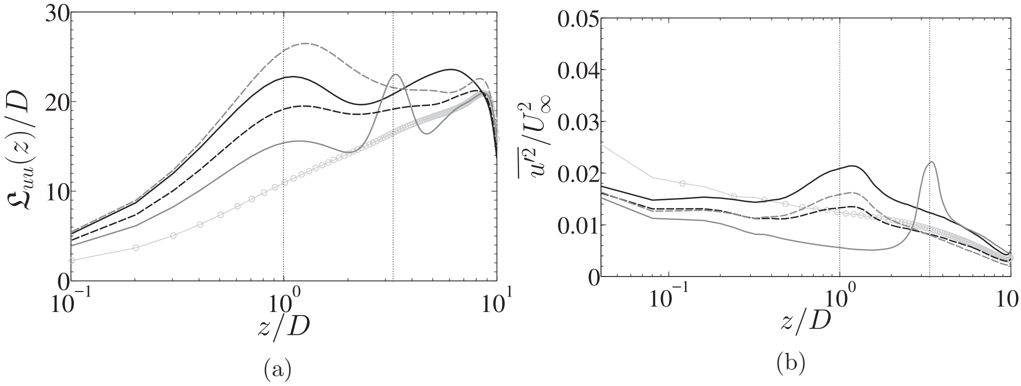

FIG. 12. Vertical variation of (a) integral length scales $\mathfrak{L}_{uu}$ based on streamwise fluctuations and (b) normalized mean-squared streamwise fluctuations $\overline{u'^2}/U_\infty^2$ (averaged over xy planes), with and without the presence of wind turbines. Solid black—Case I; dashed black—Case IIa; dashed gray—Case IIb; solid gray—Case III; light gray ○—neutral ABL, without wind turbines. Dotted lines—hub heights, $z_h = 0.1H$ (Cases I, IIa, and IIb), $z_h = 0.33H$ (Case III). See Appendix C for the definition of $\mathfrak{L}_{uu}$ used in the current study.

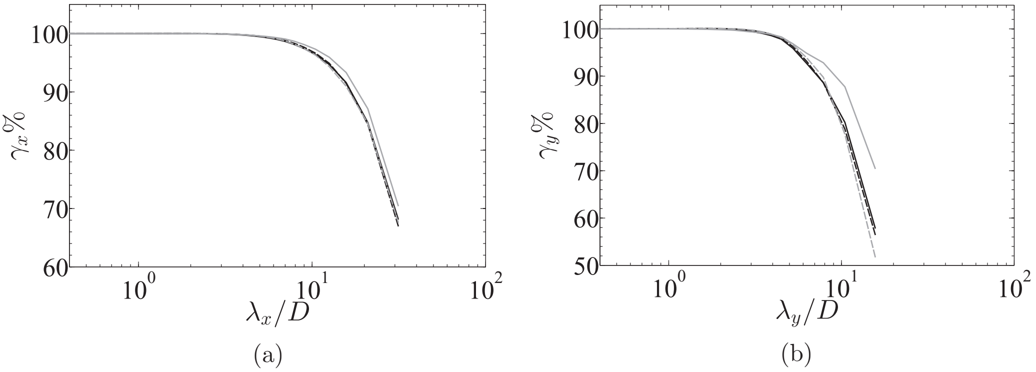

FIG. 13. Cumulative spectral content of the difference in MKE flux, $\gamma_\eta(\lambda_\eta)$ [Eq. (13)] at different (a) streamwise wavelengths, $\eta = x$, (b) spanwise wavelengths, $\eta = y$. Solid black—Case I; dashed black—Case IIa; dashed gray—Case IIb; solid gray—Case III.

cases. Nonetheless, the overall dependence of $\mathfrak{L}_{uu}(z)$ is markedly different in Case III than in other cases, showing significantly smaller length scales in the inner layer, due to a reduced influence of the enhanced turbulence structures at hub-height, that are now significantly further away, on the inner layer turbulence.

The discussions above are further corroborated by the cumulative spectral content of the MKE flux difference, γ_x,γ_y, at streamwise and spanwise length scales, for different cases (see Fig. 13). The large-scale motions with scales greater than $10D$ contain $>80\%$, even more so for streamwise motions, of the spectral flux difference, while scales smaller than $10D$ contribute to less than 20% of the spectral flux difference among the resolved scales $0.6D < \lambda_x < 60D$, $0.5D < \lambda_y < 30D$, see Appendix A for the discussion of the resolved scales. The maximum discrepancies among Cases I–III for γ_x, γ_y occur at the large length scales $>10D$, while they are almost identical for smaller scales $<4D$. Further, the maximum discrepancies in the spectral content occur between Case III and the other cases both for γ_x and γ_y, amounting to a difference of $\sim$20% in γ_y. As mentioned earlier, with the statistical uncertainty in spectra of less than 0.01% over the chosen averaging time of 50 T_e, the observed discrepancies are attributed to the physical flow features and not spectral uncertainties. This indicates that the large-scale structures, that are generated around the hub-height as seen earlier, in Case III have higher energy content than in Cases I, IIa, and IIb, probably due to the fact that they reside in the outer layer where convective velocities are higher. This can also be observed in Fig. 8, where Case III has consistently higher values of MKE flux difference at length scales $\lambda_x,\lambda_y \gtrsim 11D$. A summary of the dynamics of different length scales in our simulated wind farms is provided in Table II . These results are observed to be in line with the findings of the large-scale motions [19] of wall bounded turbulence, or the large roller-mode structures in POD of infinite wind farms [30].

TABLE II. Summary of the dynamics of important length scales in wind farms resolved by LES simulations for different Cases I–III.

Length scales ($\lambda_{x,y}$)	Dynamics
$\geqslant 10D$	Major contribution ($>80\%$) to positive $P_{\text{mean}} \sim s_x s_y D^2 \Delta\Phi_p$
$\sim D$	Small positive or negative contribution to $P_{\text{mean}} \sim s_x s_y D^2 \Delta\Phi_p$, depending on hub height z_h
$<D$	Influenced and dissipated by subgrid scale viscosity

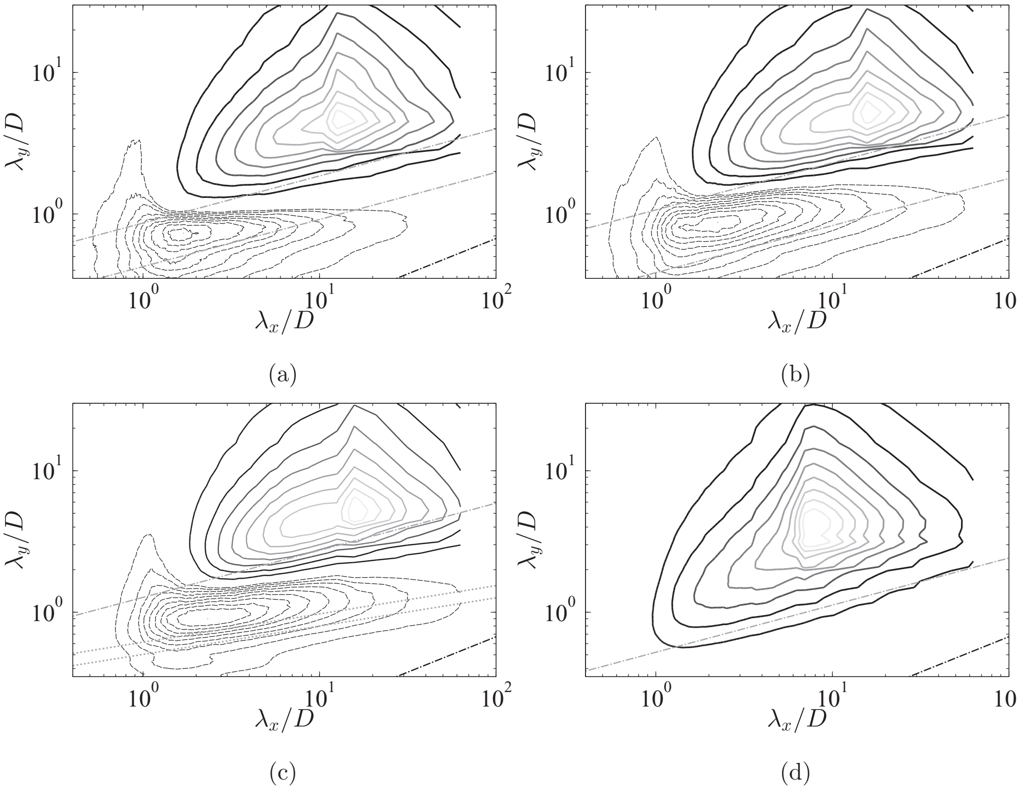

FIG. 14. 2D premultiplied spectra of the difference in MKE flux, $k_x k_y \Delta\hat{\Phi}_p(\lambda_x,\lambda_y)/U_\infty^3$, versus normalized streamwise and spanwise wavelengths. (a) Case I, (b) Case IIa, (c) Case IIb, (d) Case III. Solid gray—positive contours, dashed gray—negative contours. Chain dotted gray—$\lambda_y \sim \lambda_x^{1/3}$, chain dotted black—$\lambda_y \sim \lambda_x^{1/2}$. Gray dotted—$\lambda_y \sim \lambda_x^{1/5}$. Contour levels: positive—10 levels, from 10% to 100% of maximum; negative—10 levels from 10% to 100% of minimum.

The two-dimensional premultiplied spectral difference, $k_x k_y \Delta\widehat{\Phi}_p(\lambda_x,\lambda_y)$ in Figs. 14(a)–14(d) corroborate the discussions above made with the 1D spectra, but additionally, also contain the new information about the scaling laws and anisotropy of the eddies responsible for the MKE flux. The streamwise horizontally anisotropic ($\lambda_x \gg \lambda_y$) eddies responsible for the positive contribution of the spectra show a power law scaling of the form $\lambda_y \sim \lambda_x^{1/3}$. Cases manifesting the negative contribution of spectra (updraft), e.g., Cases I and IIa demonstrate signatures of power-law scaling $\lambda_y \sim \lambda_x^{1/3}$, and Case IIb shows $\lambda_y \sim \lambda_x^{1/5}$, which is quite different than the $1/3$ power-law dynamics. This hints towards the fact that for Case IIb, while there is an evidence of wider structures for the downdrafts, thinner intermediate scales might be responsible for the updrafts compared to Cases I and IIa. Also illustrative from the figures is the fact that the eddies responsible for the negative contribution of the spectra manifest a greater degree of horizontal anisotropy ($\lambda_x > \lambda_y$) than for the eddies accountable for the positive contribution.

The $1/3$ power law in the 2D spectra of the MKE flux difference [Figs. 14(a)–14(d)] for different cases is expectedly also present in the spectra of the MKE flux (Fig. 15), and also in the 2D u,w,uw spectra as shown in Fig. 6(b) for the different turbine layouts in Cases I–III. This justifies that the $1/3$ power law is a manifestation of coherent interactions in the flow field, which is invariant of the turbine layout. A scaling analysis is also present below, to justify the power law.

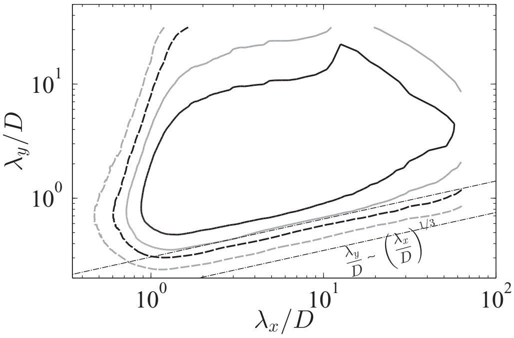

FIG. 15. 2D premultiplied spectra of MKE flux for baseline Case I at locations $z = z_h \pm D/2$. Solid—$z = z_h - D/2$, dashed—$z = z_h + D/2$. Black—25% of the maximum contour. Gray—12.5% of the maximum contour. Chain dotted black line—$\lambda_y \sim \lambda_x^{1/3}$

The width of the turbine wake, δ_y, grows in the streamwise direction, in accordance with the turbulent mixing laws in the wake region, $z_h - D/2 < z < z_h + D/2$. Assuming the width and the height of the wakes are the same for circular turbine wakes, the dispersion relation of the wake width in a background turbulence is

$$\delta_y \sim (\nu_w t_e)^{1/2}, \tag{15}$$

where ν_w can be thought of as a wake eddy viscosity corresponding to the wake mixing [9], and t_e is the lifetime of the eddies in the wake region. The streamwise convection of wakes occurs mainly as a shear layer, with the streamwise wavelengths $\lambda_x \sim S\delta_y t_e$, where S is the velocity gradient scale in the mixing length region. As shown in Fig. 16, the low velocity wake regions at hub-height location $z = z_h = 0.1H$ amidst the high velocity atmospheric turbulence impose a shear scale S due to the spanwise modulation of the streamwise flow similar to the near-wall streaks.

Consequently, substituting eddy lifetime $t_e \sim \lambda_x/(S\delta_y)$, in the turbulent dispersion relation $\delta_y \sim (\nu_w t_e)^{1/2}$ one can obtain an equation below in a nondimensional form,

$$\delta_y/D = \beta(\lambda_x/D)^{1/3}, \tag{16}$$

with spanwise length scales $\lambda_y \sim O(\delta_y)$ giving $\lambda_y/D = \beta(\lambda_x/D)^{1/3}$. A short scaling analysis reveals that the wake eddy viscosity $\nu_w \sim U_c D$ (at high Re, the lateral and normal expansion of the wake is insignificant), with the velocity scale, $U_c \sim 1/2(\langle\overline{u}\rangle|_{z_h+D/2} + \langle\overline{u}\rangle|_{z_h-D/2})$. The shear scale $S \sim \Delta U/D$ where $\Delta U = (\langle\overline{u}\rangle|_{z_h+D/2} - \langle\overline{u}\rangle|_{z_h-D/2})$. Subsequently, this gives $\beta = (U_c/\Delta U)^{1/3}$, with $\beta \approx 10$ for Cases I, IIa, IIb and $\beta \approx 80$ for Case III, as computed from the mean statistics of our

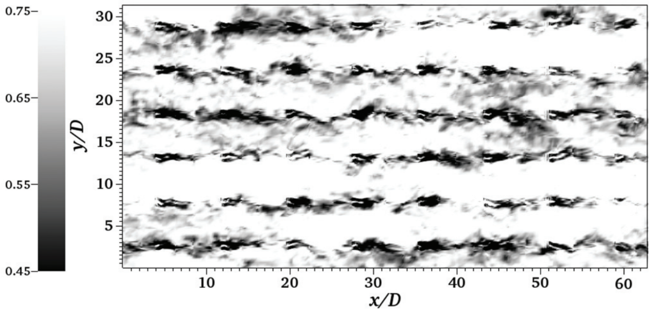

FIG. 16. Snapshot of normalized velocity magnitude $\sqrt{u^2 + v^2 + w^2}/U_\infty$ contour for Case I, in xy plane at hub-height location $z = z_h$, taken at 15 flow-through times T_e after obtaining statistical stationarity.

simulations. This illustrates that the coefficient β of the scaling law maintains the same order of magnitude for all the cases, but is conspicuously affected by the hub-height z_h of the wind farm.

IV. CONCLUSION AND FUTURE WORK

In this work we study the large-scale structures involved in the power generation of large wind farms with different geometric roughness $z_{0,\mathrm{hi}}$ (different turbine layout) in the asymptotic limit using Fourier analysis. In particular, we focus on the parametric study of increasing wind farm power by increasing the geometric roughness, from the perspective of the dynamics of the length scales in the farm. By investigating the spectra of the mean kinetic energy flux difference at the top and bottom wake region over the global computational domain, we observe that large streamwise *anisotropic eddies* of length scale $>10D$ (D is the turbine rotor diameter) that contain over 80% of the flux spectral content are responsible for the power generation in large wind farms. Rather different dynamics are observed at length scales $\sim O(D)$ for the different cases with parametric variation in s_x, s_y, z_h. For farms with lower hub-height (z_h), scales $\sim O(D)$ are also responsible for the negative contribution or the upward vertical entrainment of the MKE flux, that does not contribute to the wind turbine power.

At larger scales $\lambda_x > 30D$, the near-wall $k_x^{-1/2}$ scaling corresponding to the *attached eddies* were observed in the MKE flux as well as the flux-difference spectra. We also notice a regime of robust $1/3$ scaling law ($\lambda_y \sim \lambda_x^{1/3}$) in the 2D premultiplied MKE flux difference spectra, similar to the energy and cospectra, arising due to the background turbulent dispersion of the *wake shear layer* in the wind farm. Additionally, the two-dimensional spectra of the MKE flux difference also elucidate on the horizontal anisotropy of the eddies that make significant contribution to the power generation. In general, from the spectra of u, w energy, as well as the integral length scales it is apparent that the enlargement of eddy sizes near the wall is caused by the downdraft of vertical turbulent motions due to the mechanism of MKE flux entrainment. As a final remark, we also want to highlight about the *modulation* of large-scale structures in the wind farms, where eddies containing high amount of turbulent kinetic energy were observed near and around the hub-height location of wind farms (such nonuniform distribution of energy-containing eddies across the boundary layer was not seen in the case without the wind farms). These modulations of large-scale structures were also quantitatively estimated by computing the vertical variation of the integral length scales showing peaks in wind farm layouts when compared to neutral ABL flows without wind turbines. These effects can be potentially explored for a possibility of efficient, *symbiotic*, design of wind farms where smaller turbines are placed in between the larger ones in a vertically staggered orientation, so that an “optimized” energy harvesting can be achieved.

ACKNOWLEDGMENT

The authors T. Chatterjee and Y. T. Peet acknowledge the support of NSF-CBET Grant No. 13358568 and the compute hours from XSEDE research allocation Grants No. TG-ENG140005 and No. TG-ENG150019 for their present work.

APPENDIX A: DETAILS OF NUMERICAL GRIDS AND RESOLUTION

1. Numerical grids and grid refinement

This section presents the details of the numerical grids, their structure, and the resolution, used for the simulations discussed in the current work. Tables III and IV show a comparison of the grids used in the simulations of the neutral atmospheric boundary layer and wind farms, respectively, with that of the previous literature. While most of the previously reported numerical studies relevant to the subject used a uniform grid spacing in the context of Fourier spectral finite difference or staggered finite difference schemes, the current spectral-element based method (SEM) uses Gauss-Lobato-Legendre (GLL) quadrature point distribution which is nonuniform within the element and clusters the points towards the element boundaries. Thus, while comparing our grids to the previous studies, Δ_x, Δ_y, Δ_z

TABLE III. Comparison of various resolution parameters of spectral element neutral ABL simulations [36] with the previous literature. Sullivan *et al.* (1994)[a]—weakly convective ABL; Sullivan *et al.* (1994)[b]—neutral ABL.

Case	Geometry	N_{xyz}	Δ_x/H	Δ_y/H	Δ_z/H	Δ_x/Δ_z	Δ_y/Δ_z	Δ_x/Δ_y
Sullivan *et al.* (1994)[a] [55]	$2.6H \times 2.6H \times H$	$192 \times 192 \times 75$	0.014	0.014	0.013	1.02	1.02	1.0
Sullivan *et al.* (1994)[b] [55]	$3H \times 3H \times H$	$96 \times 96 \times 96$	0.031	0.031	0.013	2.3	2.3	1.0
Porte-Agel *et al.* (2000) [23]	$2\pi H \times 2\pi H \times H$	$54 \times 54 \times 54$	0.116	0.116	0.019	6.5	6.5	1.0
Brasseur *et al.* (2010) [25]	$3H \times 3H \times H$	$360 \times 360 \times 128$	0.008	0.008	0.008	1	1	1.0
Xie *et al.* (2013) [43]	$2H \times 2H \times H$	$96 \times 96 \times 96$	0.021	0.021	0.01	2	2	1
Meyers *et al.* (2013) [26]	$2\pi H \times \pi H \times H$	$128 \times 128 \times 96$	0.049	0.025	0.01	4.7	2.4	2.1
Verhulst *et al.* (2014) [30]	$\pi H \times \pi H \times H$	$128 \times 128 \times 61$	0.025	0.025	0.016	1.5	1.5	1
Stevens *et al.* (2015) [53]	$4\pi H \times 2\pi H \times H$	$1024 \times 512 \times 256$	0.012	0.012	0.004	3	3	1
Current ABL (PoF, 2017) [36]	$2\pi H \times \pi H \times H$	$211 \times 141 \times 169$	0.029	0.022	0.006	4.8	3.7	1.3

for the SEM is reported in the mean sense, by dividing *spectral element size* $\Delta^e_{x,y,z}$ in the x,y,z direction (which is invariant in each direction in the present ABL simulations) by the order of the Legendre polynomial p. While the grid resolution of previous neutral ABL simulations displays a considerable amount of scatter, our spectral element grid parameters appear to be consistently within the range of this scatter. Furthermore, our previous work [36] has revealed that our spectral element grid sizes were within the requirements of *High-Accuracy-Zone* of Brasseur and Wei [25], as was manifested by the proper logarithmic trends of the mean velocity profile and correct spectral scaling laws in ABL for our best-performing subgrid-scale model [36] utilized in the current work.

Along similar lines, Table IV manifests the grid resolution of periodic wind farms from the previous literature as compared against the spectral element simulations. The current wind turbine array boundary layer (WTABL) grids for all the cases were obtained by refinement of the base spectral-element ABL grid discussed above. It was thus ensured that the WTABL grids are first of all adequately resolved for correctly capturing the atmospheric boundary layer trends with LES. While most of the previous periodic wind farm simulations relied on the actuator disk models for the turbines and had uniform grid spacing, our spectral element simulations with the *actuator line model* for wind turbine blades manifests grid nonuniformity. In addition to a nonuniform clustering of GLL quadrature points within each element discussed previously, the actuator line model also requires nonuniform size of the elements in order to properly capture the helical vortices propagating downstream of the turbines [31,38]. The grid parameters Δ_x, Δ_y, Δ_z in Table IV for the SEM cases are thus defined in the *global mean* sense and represent the ratio of the domain size in a given direction to the total number of collocation points in this direction, $\Delta_\eta = L_\eta/(N^e_\eta\, p)$.

TABLE IV. Comparison of the various resolution parameters of current periodic wind farm simulations (Cases I, IIa, IIb, and III) with the previous literature. Grid parameters of Cases I, IIa, IIb, and III are defined in the global mean sense. All simulations in wind farms are performed in neutral ABL framework.

Case	Geometry	N_{xyz}	Δ_x/H	Δ_y/H	Δ_z/H	Δ_x/Δ_z	Δ_y/Δ_z	Δ_x/Δ_y
Calaf *et al.* (2010) [9]	$2\pi H \times \pi H \times H$	$128 \times 192 \times 61$	0.049	0.016	0.016	2.9	2.9	3
Verhulst *et al.* (2014) [30]	$2\pi H \times \pi H \times H$	$256 \times 128 \times 61$	0.025	0.025	0.016	1.5	1.5	1
Stevens *et al.* (2015) [8]	$6\pi H \times \pi H/2 \times H$	$1024 \times 128 \times 256$	0.019	0.012	0.004	4.7	3	1.6
I	$2\pi H \times \pi H \times H$	$379 \times 393 \times 169$	0.016	0.008	0.006	2.6	1.3	2.0
IIa	$2\pi H \times \pi H \times H$	$316 \times 393 \times 169$	0.019	0.008	0.006	3.2	1.3	2.3
IIb	$2\pi H \times \pi H \times H$	$379 \times 309 \times 169$	0.016	0.01	0.006	2.6	1.6	1.3
III	$2\pi H \times \pi H \times H$	$379 \times 393 \times 169$	0.016	0.008	0.006	2.6	1.3	2.0

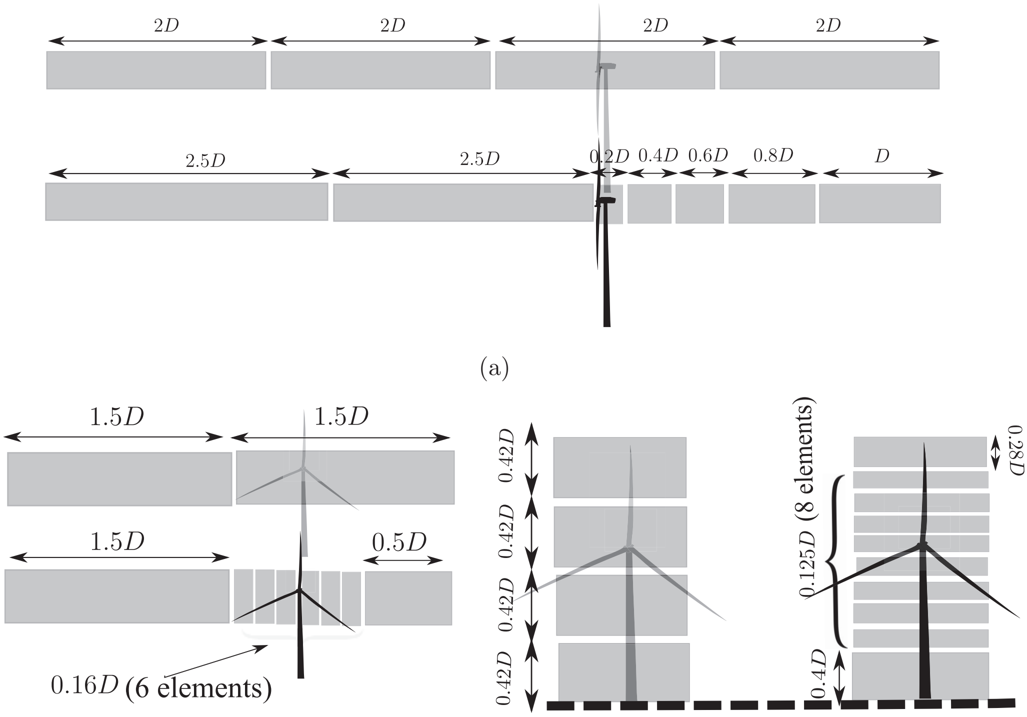

(a)

(b)

(c)

FIG. 17. Schematic of grid refinements of Case I compared to neutral ABL in the region near the WT rotors in (a) streamwise, (b) spanwise, and (c) vertical direction. Location of a hypothetical turbine (in gray) shown in the neutral ABL grid. $D = 0.1H$ is the rotor diameter. Thick dashed black line—location of the bottom rough wall surface.

2. Resolved scales in LES simulation

The refinement of the ABL grid to correspond to the periodic wind farm cases was done according to the rules described below. A schematic of the refinement of grids near the wind turbine rotors is also provided in Fig. 17. The description below follows the example of grid for Case I, while the grids for the other Cases IIa, IIb, and III are designed based on a similar logic. It must be noted that even though the neutral ABL grid has the elements of a uniform size in x, y, z directions, the location of the wind turbines is not necessarily at the *element boundaries*. Thus, in Fig. 17, the streamwise and spanwise element refinements shown are representative of all the turbine rotors in the 4th row and the 1st column, respectively. Even though the elements stretched in the streamwise and spanwise direction during the refinements of WT grids for differently located turbines may be slightly different in size, the essential idea behind the refinement remains the same as illustrated in Figs. 17(a) and 17(b). The wall-normal refinement shown in Fig. 17(c) holds for all the turbine rotors.

(a) A baseline ABL grid documented in Tables I and III is used, which utilizes $30 \times 20 \times 24$ elements with a polynomial order $p = 7$.

(b) Horizontal (streamwise) refinement of grids near WT rotor: three elements in the streamwise direction are added downstream of each of the eight turbines, while subsequently stretching only the neighboring elements as required. Total number of streamwise elements in the WT array is $30 + 8 \times 3 = 54$

(c) Horizontal (spanwise) refinement of grids near WT rotor: six elements in the spanwise direction are added in the rotor region that uniformly span the rotor-swept area of diameter D

TABLE V. Maximum and minimum grid sizes for current wind farm simulations—Cases I, IIa, IIb, and III.

Case	$\Delta_x/H\|_{\min}$	$\Delta_x/H\|_{\max}$	$\Delta_y/H\|_{\min}$	$\Delta_y/H\|_{\max}$	$\Delta_z/H\|_{\min}$	$\Delta_z/H\|_{\max}$
I	0.003	0.037	0.0024	0.023	0.0014	0.013
IIa	0.003	0.037	0.0024	0.023	0.0014	0.013
IIb	0.003	0.037	0.0024	0.023	0.0014	0.013
III	0.003	0.037	0.0024	0.023	0.0014	0.013

for six turbines in each of six rows, while subsequently stretching only the neighboring elements as required. Total number of spanwise elements in the WT array is $20 + 6 \times 6 = 56$

(d) Vertical (wall-normal) refinement of grids near WT rotor: eight elements in the vertical direction are added in the rotor region that uniformly span the rotor-swept area of diameter D for six turbines in each of six rows. While grids in the near-wall region are thus substantially refined, grids in the outer layer region are stretched proportionately (while still being in the *high-accuracy zone* [25] of vertical grids) to maintain the same number of spectral elements ($N_z^e = 24$) in the vertical direction.

Table V shows the minimum and maximum grid resolution of the current spectral element wind farm simulations, averaged over the GLL points within the element. This demonstrates that spectral elements of size that are an order of magnitude smaller are present near the "actuator lines" than in the region far away from the turbines. Note that the minimum and maximum element sizes do not depend on a case, since the element refinement and stretching is local to the turbines and does not depend on the number of turbines.

Tables IV and V illustrate that the grid sizes chosen for the current wind farm spectral element simulations are on par with the finer resolution simulations from the previous literature. Furthermore, the current exponentially accurate spectral element methodology provides nondissipative and low-dispersive numerical schemes beneficial for large eddy simulations [36], which conforms to the ideas of utilizing highly accurate numerical schemes for a proper description of turbulent interactions in WT arrays [9]. The smallest resolved length scale of the neutral ABL simulations can be defined using the Nyquist criterion as

$$\lambda_{\eta,\mathrm{resABL}} = 2\,\Delta_\eta^e/p = 2\,\Delta_\eta, \tag{A1}$$

where Δ_η^e is the element size in the η direction, p is the order of the polynomial approximation, and Δ_η is the "mean" grid size presented in Table III. This definition aims to reconcile the high-order approximation defined on spatially varying GLL points, and the classical Fourier approximation of the same resolution. It is thus seen from Table III that the smallest resolved length scale corresponds to $\lambda_{x,\mathrm{resABL}} = 0.058H = 0.58D$ and $\lambda_{y,\mathrm{resABL}} = 0.044H = 0.44D$.

For WTABL grids, the element resolution is nonuniform, and, while the largest element sizes are on par with these of the ABL grid, the resolution near the wind turbine rotors is about ten times finer, which means that the length scales that are on the order of magnitude smaller, are captured by the grid around the location of wind turbines. However, during Fourier analysis, the scale contribution is defined in a sense of a global averaging, and the spatial information is lost. In this sense, the contribution to the Fourier spectra at a particular wave number comes from the spatial regions where this wave number might be resolved, and where it might be unresolved. As a result, different physics captured in different regions of the grid is manifested as a combined effect in the spectra at wavelengths $\lambda_{x,y} < \lambda_{\eta,\mathrm{resABL}}$. Therefore, only the length scales that are adequately resolved everywhere in the computational domain can be considered reliable in the context of Fourier spectral analysis, and we thus restrict our analysis to the length scales $\lambda_x > \lambda_{x,\mathrm{resABL}} \sim 0.6D$, and $\lambda_y > \lambda_{y,\mathrm{resABL}} \sim 0.5D$ in this paper. Multiresolution features of the grid and the ability to capture different scales of motion at different spatial locations can potentially be explored with multiresoluton analysis techniques such as wavelets, and is left for the future work. Practically, the spectral analysis in the current study is accomplished by spectrally interpolating the results of the LES simulations onto a uniform grid for Fourier analysis, with 1024 × 512 gridpoints, which gives an effective Fourier grid resolution of $\Delta_\eta^F = 0.006H$, or wavelength resolution $\lambda_\eta^F = 0.012H$, that does not interfere with the resolved length scales of $\lambda > 0.05H$ as defined above. Although the scales below $\lambda < D$ are resolved by the grid, they are also affected by the SGS dissipation, as discussed in Sec. III B.

APPENDIX B: TWO POINT CORRELATIONS AND SPECTRA

1. Two-point correlations

Note that turbulence in wind turbine array boundary layers is vertically and horizontally inhomogeneous. For a given height z, we define a two point correlation between the points $\boldsymbol{x}_r = (x,\ y)$, $\boldsymbol{x}_r + \boldsymbol{r} = (x + \Delta_x, y + \Delta_y)$ through an averaging in a horizontal plane,

$$\mathfrak{R}_{u_i'u_j'}(\boldsymbol{r},t;z) = \frac{1}{L_x L_y}\iint_A \langle u_i'(\boldsymbol{x}_r,t;z)u_j'(\boldsymbol{x}_r+\boldsymbol{r},t;z)\rangle d^2\boldsymbol{x}_r. \tag{B1}$$

Here u_i' refers to the turbulent velocity fluctuations in the i^{th} direction, $A \in [-L_x/2, L_x/2] \times [-L_y/2, L_y/2]$ is the rectangular patch corresponding to the xy plane at each z location, $\langle\rangle$ denotes the ensemble average. Due to invoking of the horizontal average, the correlation $\mathfrak{R}_{u_i'u_j'}(\boldsymbol{r},t;z)$ is only a function of the point separation $\boldsymbol{r}$, and not the points themselves, $\boldsymbol{x}_r, \boldsymbol{x}_r + \boldsymbol{r}$.

For homogeneous turbulence, we can impose an equivalence between the spatial average and the ensemble average, thus recovering the classical definition of two point correlation, $\mathfrak{R}_{u_i'u_j'}(\boldsymbol{r},t;z) = \langle u_i'(\boldsymbol{x},t;z)u_j'(\boldsymbol{x}+\boldsymbol{r},t;z)\rangle$ [34]. In inhomogeneous turbulence, we need to perform a spatial averaging explicitly to recover that. Furthermore, for statistically stationary flows, the ensemble average $\langle\rangle$ can be replaced with the temporal average $\overline{}$ (due to ergodicity), as is done in the subsequent sections owing to a statistical stationarity of both ABL and WTABL flows with the temporally invariant mean wind, as considered in the current paper. This makes the two point correlation in Eq. (B1) time-invariant, as $\mathfrak{R}_{u_i'u_j'}(\boldsymbol{r};z)$.

2. Definition of spectra

The energy spectra for the inhomogeneous WTABL arrays can be defined from the Fourier transform of the two-point correlation as follows:

$$\hat{E}_{u_i'u_j'}(\boldsymbol{k_r}) = \frac{1}{2\pi}\iint_{r\in\mathbb{R}} \mathfrak{R}_{u_i'u_j'}(\boldsymbol{r};z)e^{-i\boldsymbol{k_r}\cdot\boldsymbol{r}}d^2\boldsymbol{r}, \tag{B2}$$

where $\boldsymbol{k_r}$ denotes the two dimensional wave number $\boldsymbol{k}_r = (k_x, k_y)$. Thus, the spectral content of $\mathfrak{R}_{u'u'}(\boldsymbol{r};z)$, $\mathfrak{R}_{w'w'}(\boldsymbol{r};z)$, corresponds to the streamwise and wall normal energy spectra, while that for $\mathfrak{R}_{u'w'}(\boldsymbol{r};z)$ is representative of the spectra of the kinematic shear stress (cospetra), which is required for the calculation of the MKE flux spectra in Eq. (9). The energy spectra as well as the kinematic shear stress cospectra are numerically evaluated as

$$\hat{E}_{u_i'u_j'}(\boldsymbol{k_r}) = \overline{\hat{u}_i(\boldsymbol{k_r},t;z)\hat{u}_j^*(\boldsymbol{k_r},t;z)}. \tag{B3}$$

This is an outcome of the convolution theorem, illustrating that transform of the convolution of two variables in the physical space is equal to the product or their individual transforms in the spectral space [34].

APPENDIX C: INTEGRAL LENGTH SCALES

The integral length scales can be calculated from the correlation coefficients,

$$\rho_{u_i'u_j'}(\boldsymbol{r};z) = \frac{\mathfrak{R}_{u_i'u_j'}(\boldsymbol{r};z)}{[\mathfrak{R}_{u_i'u_i'}(0,z)]^{1/2}[\mathfrak{R}_{u_j'u_j'}(0;z)]^{1/2}}, \tag{C1}$$

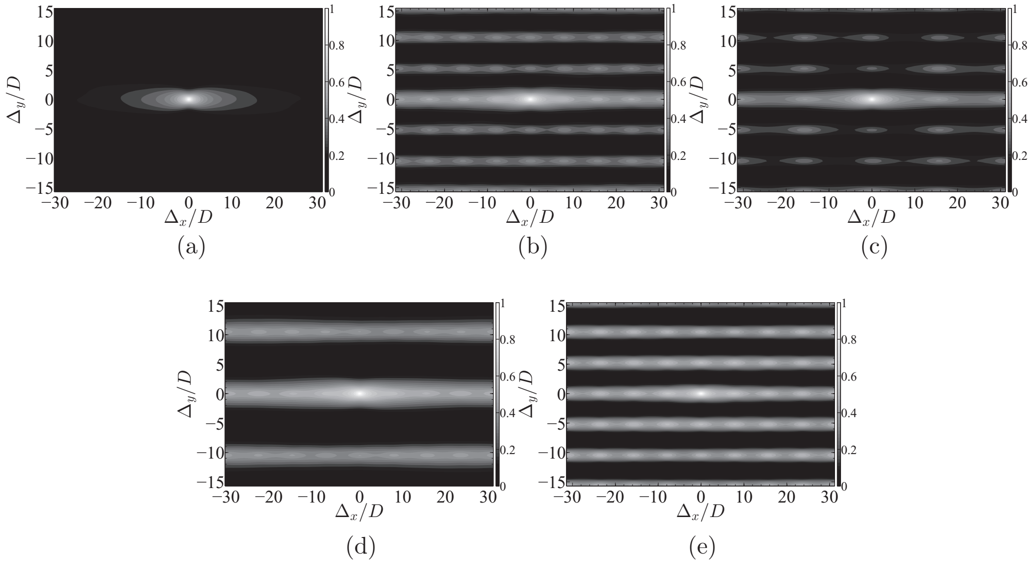

(a) (b) (c)

(d) (e)

FIG. 18. Streamwise 2D correlation coefficient $\rho_{u'u'}(\boldsymbol{r}; z = \xi)$ for flows with and without wind turbines. Panels (a)–(e) correspond to the Cases neutral ABL at $\xi = D$ and Cases I, IIa, IIb, and III at $\xi = z_h$ (hub-height), respectively.

constructed from the two-point correlations discussed in the previous section. In the current paper, for the neutral ABL and the WTABL arrays, we consider the integral length scales calculated from the correlations of the streamwise velocity fluctuations, $\rho_{u'u'}(\boldsymbol{r}; z)$, which play a dominant role in the turbulence statistics.

Figures 18 and 19 reflect the 2D correlation coefficient $\rho_{u'u'}(\boldsymbol{r}; z)$ for the wind farm Cases I, IIa, IIb, and III and the neutral ABL (without wind turbines) at two different wall-normal locations.

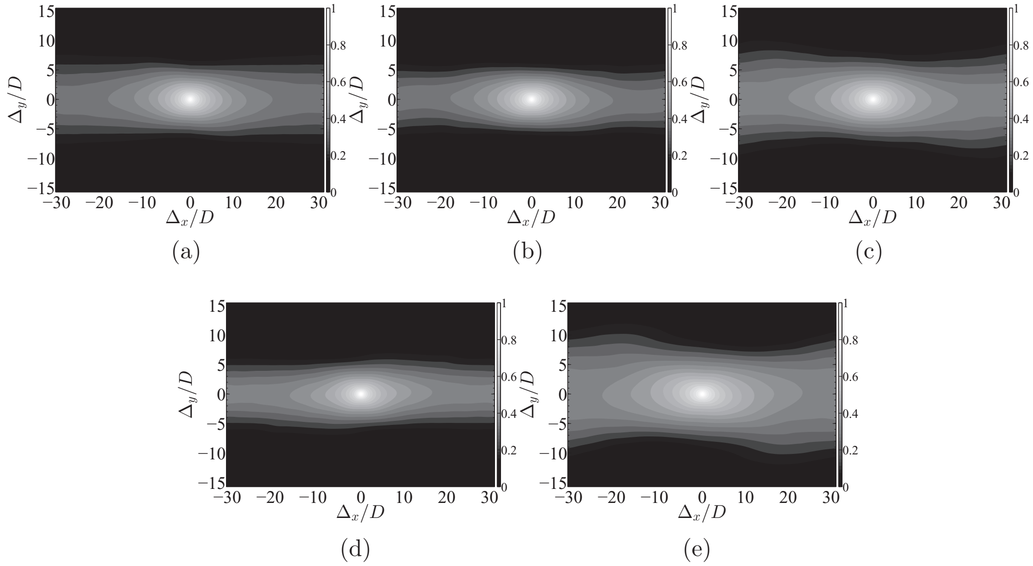

(a) (b) (c)

(d) (e)

FIG. 19. Streamwise 2D correlation coefficient $\rho_{u'u'}(\boldsymbol{r}; z = 8.75D)$ for flows with and without wind turbines. Panels (a)–(e) correspond to the Cases neutral ABL, I, IIa, IIb, and III, respectively.

While at the outer layer, $z = 8.75D$ (Fig. 19) all the wind farm layouts and neutral ABL display similar features of the gradual decay of the correlation coefficient $\rho_{u'u'}$ with increasing separations Δ_x, Δ_y, the correlation coefficient at hub-height locations of wind farms ($z = D$ for Cases I, IIa, and IIb; $z = 3.3D$ for Case III) and the neutral ABL at $z = D$, manifests remarkably different behavior. At $z = D$, the correlation coefficient of neutral ABL illustrates a single peak, while $\rho_{u'u'}$ at the hub-heights of different wind farm layouts manifests multiple peaks in line with the matrix arrangement of the wind turbines. It must be noted that similar peaks in the spectral picture were also observable in Figs. 6(a), 8, and 10.

Integral length scales in the current paper plotted in Fig. 12 are defined as

$$\mathfrak{L}_{uu}(z) = \int_{r_x \in \mathbb{R}} \rho_{u'u'}(\Delta_x, 0; z) d\Delta_x, \tag{C2}$$

by utilizing the correlation coefficient $\rho_{u'u'}(\Delta_x, 0; z)$ between the two points separated only at the streamwise direction, at the same spanwise location y. As can be seen from Figs. 18 and 19, this definition of length scales, from choosing two points $\boldsymbol{x}_r = (x, y), \boldsymbol{x}_r + \boldsymbol{r} = (x + \Delta_x, y)$ at a fixed spanwise location in the construction of the two point correlation in Eq. (B1), and subsequently the correlation coefficient, while averaging in the spanwise direction, yields the upper bound on length scales owing to highly correlated motions in the presence of streamwise dynamics. The contours of $\rho_{u'u'}$ further help us understand the reason for the modulation of integral length scales in the wind farms compared to the neutral ABL (without turbines).

[1] F. Porté-Agel, Y.-T. Wu, and R. J. Conzemius, Large-eddy simulation of atmospheric boundary layer flow through wind turbines and wind farms, J. Wind Eng. Ind. Aerodynam. **99**, 154 (2011).

[2] M. J. Churchfield, S. Lee, P. J. Moriarty, L. A. Martinez, S. Leonardi, G. Vijayakumar, and J. G. Brasseur, *A Large-Eddy Simulation of Wind-Plant Aerodynamics*, AIAA Paper 2012-0537 (2012).

[3] C. L. Archer, S. Mirzaeisefat, and S. Lee, Quantifying the sensitivity of wind farm performance to array layout options using large-eddy simulation, Geophys. Res. Lett. **40**, 4963 (2013).

[4] G. Mosetti, C. Poloni, and B. Diviacco, Optimization of wind turbine positioning in large windfarms by means of a genetic algorithm, J. Wind Eng. Ind. Aerodynam. **54**, 105 (1994).

[5] J. Meyers and C. Meneveau, Optimal turbine spacing in fully developed wind-farm boundary layers, Wind Energy **15**, 305 (2012).

[6] Y.-T. Wu and F. Porté-Agel, Simulation of turbulent flow inside and above wind farms: Model validation and layout effects, Boundary Layer Metereol. **146**, 181 (2013).

[7] L. P. Chamorro, N. Tobin, R. E. A Arndt, and F. Sotiropoulos, Variable-sized wind turbines are a possibility for wind farm optimization, Wind Energy **17**, 1483 (2014).

[8] R. J. A. M. Stevens, D. F. Gayme, and C. Meneveau, Effects of turbine spacing on the power output of extended wind-farms, Wind Energy **19**, 359 (2016).

[9] M. Calaf, C. Meneveau, and J. Meyers, Large eddy simulation study of fully developed wind-turbine array boundary layers, Phys. Fluids **22**, 015110 (2010).

[10] Y.-T. Wu and F. Porté-Agel, Large-eddy simulation of wind-turbine wakes: Evaluation of turbine parametrisations, Boundary Layer Metereol. **138**, 345 (2011).

[11] P. K. Jha, E. P. N. Duque, J. L. Bashioum, and S. Schmitz, Unraveling the mysteries of turbulence transport in a wind farm, Energies **8**, 6468 (2015).

[12] T. Chatterjee and Y. Peet, *Spectra and Large Eddy Structures in the Double Log-layer in a High Re Wind Turbine Array Boundary Layer*, ASME Turbo Expo GT2016-56359 (2016).

[13] N. Hamilton, H. S. Kang, C. Meneveau, and R. B. Cal, Statistical analysis of kinetic energy entrainment in a model wind turbine array boundary layer, J. Renewable Sustainable Energy **4**, 063105 (2012).

[14] J. Jiménez and J. C. del Álamo, Very large anisotropic scales in turbulent wall-bounded flows, in *Statistical Theories and Computational Approaches to Turbulence*, edited by Y. Kaneda and T. Gotoh (Springer, Japan, 2003), pp. 105–112.

[15] K. G. Mcnaughton, Attached eddies and production spectra in atmospheric logarithmic layer, Boundary Layer Metereol. **111**, 1 (2004).

[16] G. J. Kunkel and I. Marusic, Study of the near-wall-turbulent region of the high-Reynolds- number boundary layer using an atmospheric flow, J. Fluid Mech. **548**, 375 (2006).

[17] M. Guala, Large-scale and very-large-scale motions in turbulent pipe flow, J. Fluid Mech. **554**, 521 (2006).

[18] R. J. Adrian, Hairpin vortex organization in wall turbulence, Phys. Fluids **19**, 041301 (2007).

[19] B. J. Balakumar and R. J. Adrian, Large and very-large-scale motions in channel and boundary-layer flows, Philos. Trans. R. Soc. **365**, 665 (2007).

[20] J. Lee, J. Ahn, and H. J. Suang, Comparison of large- and very-large-scale motions in turbulent pipe and channel flows, Phys. Fluids **27**, 025101 (2015).

[21] C. Ver Hulst and C. Meneveau, Altering kinetic energy entrainment in large eddy simulations of large wind farms using unconventional wind turbine actuator forcing, Energies **8**, 370 (2015).

[22] J. Meyers and C. Meneveau, Flow visualization using momentum and energy transport tubes and applications to turbulent flow in wind farms, J. Fluid Mech. **715**, 335 (2013).

[23] F. Porté-Agel, C. Meneveau, and M. B Parlange, A scale-dependant dynamics model for large eddy simulation: Application to a neutral atmospheric boundary layer, J. Fluid Mech. **415**, 261 (2000).

[24] E. Bou-Zeid, C. Meneveau, and M. Parlange, A scale-dependant Lagrangian dynamic model for large eddy simulation of complex turbulent flows, Phys. Fluids **17**, 025105 (2005).

[25] J. G. Brasseur and T. Wei, Designing large eddy simulation of turbulent boundary layer to capture law-of-wall scaling, Phys. Fluids **22**, 021303 (2010).

[26] P. Wu and J. Meyers, A constraint for subgrid-scale stresses in the logarithmic region of high Reynolds number turbulent boundary layers: A solution to log-layer mismatch problem, Phys. Fluids **25**, 015104 (2013).

[27] S. Frandsen, R. Barthelmie, S. Pryor, O. Rathmann, S. Larsen, J. Hojstrup, and M. Thogersen, Analytical modeling of wind speed deficit in large offshore wind farms, Wind Energy **9**, 39 (2006).

[28] R. B. Cal, J. Lebrón, L. Castillo, H. S. Kang, and C. Meneaveau, Experimental study of the horizontally averaged flow structure in a model wind-turbine array boundary layer, J. Renew. Sustain. Energy **2**, 013106 (2010).

[29] J. Lébron, R. B. Cal, H. Kand, L. Castillo, and C. Meneveau, Interaction Between Wind Turbine Array and Turbulent Boundary Layer, Tech. Rep. (2009), 11th Americas Conference on Wind Engineering, San Juan, Puerto Rico, 22–26 June, 2009.

[30] C. Ver Hulst and C. Meneveau, Large eddy simulation study of the kinetic energy entrainment by energetic turbulent flow structures in large wind farms, Phys. Fluids **8**, 025113 (2014).

[31] N. Troldborg, Actuator line modeling of wind turbine wakes, Ph.D. thesis, Technical University of Denmark (2008).

[32] P. Fischer, J. Lottes, D. Pointer, and A. Siegel, Petascale algorithms for reactor hydrodynamics, J. Phys.: Conf. Ser. **125**, 012076 (2008).

[33] M. O. Deville, P. F. Fischer, and E. H. Mund, *High-Order Methods for Incompressible Fluid Flow* (Cambridge University Press, Cambridge, UK, 2002).

[34] Stephen B. Pope, *Turbulent Flows* (Cambridge Press, Cambridge, 2000).

[35] P. J. Mason and D. J. Thompson, Stochastic backscatter in large-eddy simulations of boundary layers, J. Fluid Mech. **242**, 51 (1992).

[36] T. Chatterjee and Y. T. Peet, Effect of artificial length scales in large eddy simulation of neutral atmospheric boundary layer flow: A simple solution to log-layer mismatch, Phys. Fluids **29**, 075175 (2017).

[37] A. S. Monin and A. M. Obukhov, Basic laws of turbulent mixing in the ground layer of the atmosphere, Trans. Geophys. Inst. Akad. Nauk. USSR **151**, 1963 (1954).

[38] T. Chatterjee and Y. Peet, Actuator Line Wind Turbine Simulations in Atmospheric Turbulent Flows using Spectral Element Method, AIAA paper 2015–0727 (2015) 5–9 January 2015, Kissimmmee, FL.

[39] J. W. Deardorff, A numerical study of three-dimensional turbulent channel flow at large Reynolds number, J. Fluid Mech. **41**, 453 (1970).

[40] U. Schumann, Subgrid scale model for finite difference simulations of turbulent flows in plane channels and annuli, J. Comput. Phys. **18**, 376 (1975).

[41] W. Cabot and P. Moin, Approximate wall boundary conditions in the large-eddy simulation of high Reynolds number flow, Flow, Turbul. Combust. **63**, 269 (2000).

[42] U. Piomelli and E. Balaras, Wall-layer models for large eddy simulations, Annu. Rev. Fluid Mech. **34**, 349 (2002).

[43] S. Xie, C. L. Archer, N. Ghaisas, and C. Meneveau, Benefits of collocating vertical-axis and horizontal-axis wind turbines in large wind farms, Wind Energy **20**, 45 (2017).

[44] H. Lettau, Note on aerodynamic roughness-parameter estimation on the basis of roughness-element description, J. Appl. Meteorol. **8**, 828 (1969).

[45] A. A. Townsend, Equilibrium layers and wall turbulence, J. Fluid Mech. **11**, 97 (1961).

[46] A. E. Perry, S. Henbest, and M. S. Chong, Theoretical and experimental studies of wall turbulence, J. Fluid Mech. **165**, 163 (1986).

[47] T. B. Nickels, I. Marusic, S. Hafez, and M. S. Chong, Evidence of the k^{-1} Law in a High-Reynolds-Number Turbulent Boundary Layer, Phys. Rev. Lett. **95**, 074501 (2005).

[48] N. Hutchins, T. B. Nickels, I. Marusic, and M. S. Chong, Hot-wire spatial resolution issues in wall-bounded turbulence, J. Fluid Mech. **635**, 103 (2009).

[49] J. Jiménez, J. Del Álamo, and O. Flores, The large-scale dynamics of near-wall turbulence, J. Fluid Mech. **505**, 179 (2004).

[50] Y. T. Peet and T. Chatterjee, The contribution of large-scale structures in the power generation of finite scale wind farms using large eddy simulation, *Proceedings of the 10th International Symposium on Turbulence and Shear Flow Phenomena (TSFP'17), Chicago, IL, July, 2017*, http://www.tsfp-conference.org/proceedings/2017/2/292.pdf.

[51] S. Hoyas and J. Jiménez, Reynolds number effects on the Reynolds-stress budgets in turbulent channels, Phys. Fluids **20**, 101511 (2008).

[52] J. Del Álamo, J. Jiménez, P. Zandonade, and R. Moser, Scaling of the energy spectra of turbulent channels, J. Fluid Mech. **500**, 135 (2004).

[53] R. Stevens, M. Wilczek, and C. Meneveau, Large-eddy simulation study of the logarithmic law for second and higher-order moments in turbulent wall-bounded flow, J. Fluid Mech. **747**, 888 (2014).

[54] R. J. Adrian, C. D. Meinhart, and C. D. Tomkins, Vortex organization in the outer region of the turbulent boundary layer, J. Fluid Mech. **422**, 1 (2000).

[55] P. P. Sullivan, J. C. McWilliams, and C. H. Moeng, subgrid-scale model for large-eddy simulation of planetary boundary-layer flows, Boundary-Layer Met. **71**, 247 (1997).